Computing edge stress intensity functions (ESIFs) along circular 3-D edges

Zohar YOSIBASH and Samuel SHANNON

Pearlstone Center for Aeronautical Eng. Studies, Dept. of Mechanical Engineering, Ben-Gurion University of the Negev, Beer-Sheva, 84105, Israel

Abstract

A newly developed method, named the quasi-dual function method (QDFM) is proposed for extracting edge stress intensity functions (ESIFs) along circular crack fronts from finite element solutions, in a general three-dimensional domain and boundary conditions. The mathematical machinery developed in the framework of the Laplace operator in [17] is extended here to the elasticity system and applied for the extraction of ESIFs from high-order finite element solutions.

The QDFM has several important advantages: a) It allows to extract the ESIFs away from the singular edge, thus avoiding the need for a refined FE mesh, b) The ESIFs are obtained as a function along the edge and not as pointwise values, c) The method is general in the sense that it is applicable to any circular edge (be it a penny shaped crack, a cylindrical crack or a circular external crack). Numerical examples are provided that demonstrate the efficiency, robustness and high accuracy of the proposed QDFM.

Keywords: Quasi-dual function method, edge stress intensity functions, penny-shaped crack, 3-D singularities

1. Introduction

Solutions of the elasticity system in two dimensional domains in the vicinity of crack tips in isotropic materials have been investigated for over half a century. These are described in terms of special singular functions depending on the geometry and the boundary conditions on crack sides, and of unknown coefficients known as stress intensity factors (SIFs) depending on the boundary conditions away from the singularities, see e.g. [20].

Although being much more realistic, three dimensional singularities have been scarcely addressed because of their complexity. In three dimensional domains like polyhedra, both vertex and edge singularities exist, see [5, 19]. For cracks in 3-D domains with a straight crack front explicit representation of the solution in the vicinity

Email address: zohary@bgu.ac.il (Zohar YOSIBASH and Samuel SHANNON)

of edges is available as a series [8, 4, 15, 21]. The functional representation of the solution was extended in [22] to circular singular edges (a "penny-shaped crack" being a special renown case) in 3-D domains. Explicit singular series expansion was provided for circular crack fronts, characterized by:

- an *exponent* α_k which belongs to a discrete set $0, 0, 0, 1/2, 1/2, 1/2, 1, 1, 1, 3/2...$ which determine the level of non-smoothness of the singularity.
- *eigenfunctions* and two families of *shadows* $\phi_{\ell,k,i}(\varphi)$ computed by solving a set of 1-D problems.
- a *function* along the edge, denoted by $A_k(\theta)$ (θ is a coordinate along the crack front) and called "Edge Stress Intensity Function" ESIF which determines the "amount of energy" residing in each singularity.

Under axisymmetric boundary conditions and geometry we have shown that our solution reduces to the one presented in [12].

From the engineering perspective the ESIFs $A_k(\theta)$ when $\alpha_k < 1$ are of major importance because these are correlated to failure initiation. Having the explicit representation of the singular solution in the vicinity of a circular edge we aim at computing these ESIFs. To this end we extended the quasidual function method (QDFM) presented in the framework of 3-D straight edges in [4, 15] to circular edges in the framework of the Laplace equation in [17]. This is because the Laplace equation is a simpler elliptic operator that allows more transparent analytic computations and invokes all necessary characteristics of the elasticity system. The QDFM was demonstrated to be an accurate and efficient method that is capable of extracting a functional approximation of EFIFs (edge flux intensity functions) along the circular edge and whose accuracy could be adaptively improved. It may be implemented as a post-solution operation in conjunction with the p -version of the finite element method. The mathematical machinery developed in the framework of the Laplace operator is extended here for the elasticity system.

To the best of our knowledge no methods are available for extracting ESIFs as functions along circular crack fronts in general domains under general loading conditions. The only ones that are known to the authors are the one by Leblond&Torlai [11] that provides the machinery for the pointwise derivation of the solution up to second order for a general curved crack. Other pointwise methods rely on the 3-D J-integral and connect its value to ESIFs using plane-strain assumptions (which are not in general valid), see e.g. [14] and the references therein. The contour integral method has also been used for the pointwise extraction of the ESIFs and is shown to predict accurate values as the integration radius tends to zero [23]. Here, we present a different approach enabling the computation of any ESIF for any circular edge be it in an axi-symmetric or non-axisymmetric setting. Furthermore the ESIFs are provided as functions along circular crack fronts, and not only as pointwise values along the edge.

The point of departure is the introduction of the QDFM for the elasticity system in section 2 with a brief sketch of the mathematical analysis on its theoretical performance. The connection between the QDFM and the ESIFs for the axisymmetric case is addressed in section 3. By analytical mathematical derivations we demonstrate the

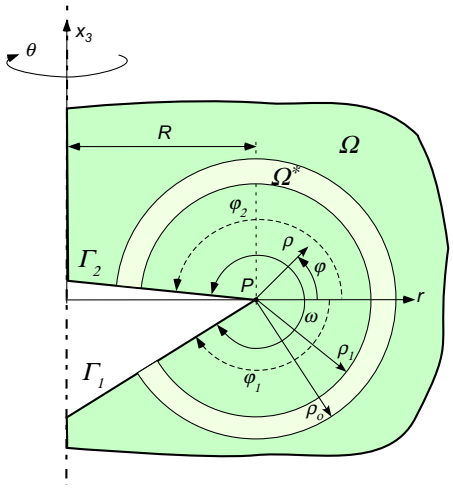

Figure 1: 3-D domain of interest Ω and the (ρ, φ, θ) coordinate system.

anticipated convergence rates of the ESIFs when extracted from analytical solutions in axisymmetric cases. Numerical examples employing the p-version of the finite element method are provided to demonstrate the efficiency of the QDFM in practical applications. Penny-shaped, cylindrical shaped and outer circular cracks are addressed. We then extend the QDFM to non-axisymmetric cases in section 4. As shall be demonstrated, the QDFM allows one to extract the ESIFs away from the singular edge, thus enables the use of coarse meshes and alleviates the necessity of complex refined mesh generation in the vicinity of 3-D singular edges. The obtained results are both accurate, efficient and robust. We summarize our results in section 5.

2. The area integral on the surface of a torus along a circular edge in 3-D domains

Consider a three-dimensional domain made of an isotropic elastic material having a circular singular edge (a penny-shaped crack front for example) of radius R. The domain may be subject to loads or displacements on its boundary away from the singular edge and free of body forces. We assign the coordinate system (ρ, φ, θ) along the circular edge shown in Fig 1. The vector $\boldsymbol{u} = (u_\rho, u_\varphi, u_\theta)^T$ denotes the three displacements in ρ, φ, θ coordinates, and λ, μ denote the two Lamé coefficients.

For sake of simplicity we restrict our attention to traction-free boundary conditions on the faces intersecting at the singular edge. The displacements in the vicinity of the singular circular edge are given as an asymptotic series of primal eigenfunctions $\boldsymbol{\phi}_{0,k,0}$ (which are the familiar 2-D eigenfunctions) and two families of shadow functions $\boldsymbol{\phi}_{\ell,k,i}$ (one family is associated with the index ℓ and the other with the index i), see details in [22]:

$$\boldsymbol{u} = \sum_{\ell=0}^{\infty}\sum_{k=0} \partial_\theta^\ell A_k(\theta)\, \rho^{\alpha_k} \sum_{i=0}^{\infty} \left(\frac{\rho}{R}\right)^{i+\ell} \begin{Bmatrix} \phi^\rho(\varphi) \\ \phi^\varphi(\varphi) \\ \phi^\theta(\varphi) \end{Bmatrix}_{\ell,k,i} = \sum_{\ell=0}^{\infty}\sum_{k=0} \partial_\theta^\ell A_k(\theta)\, \rho^{\alpha_k} \sum_{i=0}^{\infty} \left(\frac{\rho}{R}\right)^{i+\ell} \boldsymbol{\phi}_{\ell,k,i} \quad (1)$$

One may observe that for a straight crack front $R \to \infty$, only the term $i = 0$ remains in the summation on i in (1) that is equal to 1 and θ becomes the coordinate along the crack front. Furthermore $A_k(\theta)$ is constant in case of a 2-D assumption, thus the sum on ℓ vanishes, and one obtains the 2-D well known series expansion:

$$\begin{pmatrix} u_\rho \\ u_\varphi \end{pmatrix} = \sum_{k=0} A_k \, \rho^{\alpha_k} \begin{Bmatrix} \phi^\rho(\varphi) \\ \phi^\varphi(\varphi) \end{Bmatrix}_{0,k,0}$$

We concentrate our attention to the case of a crack (although the analysis equally holds for any other opening angle), so that the eigenvalues are $\alpha_{0_1} = 0, \alpha_{0_2} = 0, \alpha_{0_3} = 0, \alpha_1 = 1/2, \alpha_2 = 1/2, \alpha_3 = 1/2, \cdots$. In this case explicit expressions for the eigenfunctions $\boldsymbol{\phi}_{0,k,0}$ and their shadows $\boldsymbol{\phi}_{\ell,k,i}$ for a penny-shaped, a cylindrical and an outer circular cracks are too lengthy to be provided in an appendix and thus are provided in [16].

The stress tensor is easily obtained from (1) using the kinematic connections and Hooke's law. To relate the GESIFs A_k s to the engineering common terminology of edge stress intensity functions, we define:

$$A_1(z) = -\frac{1}{4}\frac{K_I(z)}{\mu\sqrt{2\pi}}, A_2(z) = \frac{3}{4}\frac{K_{II}(z)}{\mu\sqrt{2\pi}}, A_3(z) = 2\frac{K_{III}(z)}{\mu\sqrt{2\pi}}$$

and with this terminology the stress vector is explicitly given in [22, equation (95)]:

$$
\begin{Bmatrix} \sigma_{\rho\rho} \\ \sigma_{\theta\theta} \\ \sigma_{\varphi\varphi} \\ \sigma_{\rho\theta} \\ \sigma_{\rho\varphi} \\ \sigma_{\theta\varphi} \end{Bmatrix}
= \frac{K_I(\theta)}{\sqrt{2\pi\rho}} \left[\begin{pmatrix} -5\cos\frac{\varphi}{2} + \cos\frac{3\varphi}{2} \\ -\frac{4\lambda}{\lambda+\mu}\cos\frac{\varphi}{2} \\ -3\cos\frac{\varphi}{2} - \cos\frac{3\varphi}{2} \\ 0 \\ -\sin\frac{\varphi}{2} - \sin\frac{3\varphi}{2} \\ 0 \end{pmatrix} + \left(\frac{\rho}{R}\right) \begin{pmatrix} -\frac{5\lambda+13\mu}{4(\lambda+\mu)}\cos\frac{\varphi}{2} + \frac{\lambda+9\mu}{4(\lambda+\mu)}\cos\frac{3\varphi}{2} \\ -\frac{2(2\lambda+\mu)(\lambda+5\mu)}{(\lambda+\mu)^2}\cos\frac{\varphi}{2} + \frac{3\lambda+2\mu}{\lambda+\mu}\cos\frac{3\varphi}{2} \\ -\frac{3(\lambda+9\mu)}{4(\lambda+\mu)}\cos\frac{\varphi}{2} - \frac{\lambda+9\mu}{4(\lambda+\mu)}\cos\frac{3\varphi}{2} \\ 0 \\ \frac{\lambda-7\mu}{4(\lambda+\mu)}\sin\frac{\varphi}{2} + \frac{\lambda-7\mu}{4(\lambda+\mu)}\sin\frac{3\varphi}{2} \\ 0 \end{pmatrix} \right. \tag{2}
$$

$$
\left. + \left(\frac{\rho}{R}\right)^2 \begin{pmatrix} -\frac{-33\lambda^2+430\lambda\mu+335\mu^2}{96(\lambda+\mu)^2}\cos\frac{\varphi}{2} - \frac{21\lambda^2+154\lambda\mu+53\mu^2}{36(\lambda+\mu)^2}\cos\frac{3\varphi}{2} + \frac{311\lambda-5\mu}{32(\lambda+\mu)}\cos\frac{5\varphi}{2} \\ \frac{\mu(23\lambda+19\mu)}{2(\lambda+\mu)^2}\cos\frac{\varphi}{2} - \frac{2(4\lambda+3\mu)\left(-3\lambda^2-10\lambda\mu+\mu^2\right)}{9(\lambda+\mu)^3}\cos\frac{3\varphi}{2} - \frac{3(5\lambda+4\mu)}{8(\lambda+\mu)}\cos\frac{5\varphi}{2} \\ \frac{111\lambda^2+142\lambda\mu-97\mu^2}{96(\lambda+\mu)^2}\cos\frac{\varphi}{2} + \frac{-3\lambda^2+74\lambda\mu+61\mu^2}{36(\lambda+\mu)^2}\cos\frac{3\varphi}{2} - \frac{3(3\lambda-13\mu)}{32(\lambda+\mu)}\cos\frac{5\varphi}{2} \\ 0 \\ \frac{105\lambda^2+322\lambda\mu+89\mu^2}{96(\lambda+\mu)^2}\sin\frac{\varphi}{2} + \frac{3\lambda^2+38\lambda\mu+19\mu^2}{12(\lambda+\mu)^2}\sin\frac{3\varphi}{2} + \frac{3(-9\lambda+7\mu)}{32(\lambda+\mu)}\sin\frac{5\varphi}{2} \\ 0 \end{pmatrix} + \cdots \right]
$$

$$
+ \frac{K_I'(\theta)}{\sqrt{2\pi\rho}} \left(\frac{\rho}{R}\right) \left[\begin{pmatrix} 0 \\ 0 \\ 0 \\ \frac{2(\lambda-\mu)}{\lambda+\mu}\cos\frac{\varphi}{2} - \frac{2(\lambda+3\mu)}{\lambda+\mu}\cos\frac{3\varphi}{2} \\ 0 \\ \frac{2(\lambda+3\mu)}{\lambda+\mu}\sin\frac{\varphi}{2} + \frac{2(\lambda+3\mu)}{\lambda+\mu}\sin\frac{3\varphi}{2} \end{pmatrix} \right.
$$

$$
\left. + \left(\frac{\rho}{R}\right) \begin{pmatrix} 0 \\ 0 \\ 0 \\ \frac{9\lambda^2+96\lambda\mu+71\mu^2}{6(\lambda+\mu)^2}\cos\frac{\varphi}{2} - \frac{3(3\lambda+\mu)}{2(\lambda+\mu)}\cos\frac{3\varphi}{2} + \frac{9\lambda^2+24\lambda\mu+7\mu^2}{3(\lambda+\mu)^2}\cos\frac{5\varphi}{2} \\ 0 \\ \frac{(9\lambda+\mu)(3\lambda+5\mu)}{6(\lambda+\mu)^2}\sin\frac{\varphi}{2} + \frac{3(\lambda-\mu)}{2(\lambda+\mu)}\sin\frac{3\varphi}{2} - \frac{9\lambda^2+24\lambda\mu+7\mu^2}{3(\lambda+\mu)^2}\sin\frac{5\varphi}{2} \end{pmatrix} + \cdots \right]
$$

$$
+ \frac{K_I''(\theta)}{\sqrt{2\pi\rho}} \left(\frac{\rho}{R}\right)^2 \begin{pmatrix} \frac{-3\lambda+5\mu}{6(\lambda+\mu)}\cos\frac{\varphi}{2} + \frac{21\lambda+61\mu}{18(\lambda+\mu)}\cos\frac{3\varphi}{2} \\ \frac{2(3\lambda+2\mu)}{\lambda+\mu}\cos\frac{\varphi}{2} - \frac{4(4\lambda+3\mu)(3\lambda+7\mu)}{9(\lambda+\mu)^2}\cos\frac{3\varphi}{2} \\ \frac{3\lambda-5\mu}{6(\lambda+\mu)}\cos\frac{\varphi}{2} + \frac{3\lambda-5\mu}{18(\lambda+\mu)}\cos\frac{3\varphi}{2} \\ 0 \\ -\frac{3\lambda+11\mu}{6(\lambda+\mu)}\sin\frac{\varphi}{2} - \frac{3\lambda+11\mu}{6(\lambda+\mu)}\sin\frac{3\varphi}{2} \\ 0 \end{pmatrix} + \cdots
$$

$$
+ \frac{K_{II}(\theta)}{\sqrt{2\pi\rho}} \left[\begin{pmatrix} -\frac{5}{3}\sin\frac{\varphi}{2} + \sin\frac{3\varphi}{2} \\ -\frac{4\lambda}{3(\lambda+\mu)}\sin\frac{\varphi}{2} \\ -\sin\frac{\varphi}{2} - \sin\frac{3\varphi}{2} \\ 0 \\ \frac{1}{3}\left(\cos\frac{\varphi}{2} + 3\cos\frac{3\varphi}{2}\right) \\ 0 \end{pmatrix} + \left(\frac{\rho}{R}\right) \begin{pmatrix} -\frac{51\lambda+107\mu}{60(\lambda+\mu)}\sin\frac{\varphi}{2} + \frac{\lambda+9\mu}{12(\lambda+\mu)}\sin\frac{3\varphi}{2} \\ \frac{2\left(34\lambda^2+83\lambda\mu+45\mu^2\right)}{15(\lambda+\mu)^2}\sin\frac{\varphi}{2} + \frac{3\lambda+2\mu}{3(\lambda+\mu)}\sin\frac{3\varphi}{2} \\ -\frac{\lambda+9\mu}{12(\lambda+\mu)}\sin\frac{\varphi}{2} - \frac{\lambda+9\mu}{12(\lambda+\mu)}\sin\frac{3\varphi}{2} \\ 0 \\ -\frac{23\lambda+31\mu}{60(\lambda+\mu)}cos\frac{\varphi}{2} + \frac{-\lambda+7\mu}{12(\lambda+\mu)}\cos\frac{3\varphi}{2} \\ 0 \end{pmatrix} \right.
$$

$$
\left. + \left(\frac{\rho}{R}\right)^2 \begin{pmatrix} -\frac{1983\lambda^2+6126\lambda\mu+4015\mu^2}{1440(\lambda+\mu)^2}\sin\frac{\varphi}{2} + \frac{2121\lambda^2+5490\lambda\mu+3161\mu^2}{1260(\lambda+\mu)^2}\sin\frac{3\varphi}{2} + \frac{11\lambda-5\mu}{32(\lambda+\mu)}\sin\frac{5\varphi}{2} \\ \frac{72\lambda^2+207\lambda\mu+131\mu^2}{30(\lambda+\mu)^2}\sin\frac{\varphi}{2} - \frac{2\left(420\lambda^3+1413\lambda^2\mu+1482\lambda\mu^2+497\mu^3\right)}{315(\lambda+\mu)^3}\sin\frac{3\varphi}{2} - \frac{5\lambda+4\mu}{8(\lambda+\mu)}\sin\frac{5\varphi}{2} \\ -\frac{177\lambda^2+1074\lambda\mu+1025\mu^2}{1440(\lambda+\mu)^2}\sin\frac{\varphi}{2} - \frac{39\lambda^2+78\lambda\mu+55\mu^2}{180(\lambda+\mu)^2}\sin\frac{3\varphi}{2} - \frac{3\lambda-13\mu}{32(\lambda+\mu)}\sin\frac{5\varphi}{2} \\ 0 \\ -\frac{777\lambda^2+2178\lambda\mu+1273\mu^2}{1440(\lambda+\mu)^2}\cos\frac{\varphi}{2} + \frac{399\lambda^2+1006\lambda\mu+591\mu^2}{420(\lambda+\mu)^2}\cos\frac{3\varphi}{2} + \frac{9\lambda-7\mu}{32(\lambda+\mu)}\cos\frac{5\varphi}{2} \end{pmatrix} + \cdots \right]
$$

$$+\frac{K'_{II}(\theta)}{\sqrt{2\pi\rho}}\left(\frac{\rho}{R}\right)\left[\begin{pmatrix}0\\0\\0\\\frac{2(\lambda-\mu)}{3(\lambda+\mu)}\sin\frac{\varphi}{2}+\sin\frac{3\varphi}{2}\\0\\-\frac{2(\lambda+3\mu)}{3(\lambda+\mu)}\cos\frac{\varphi}{2}+\cos\frac{3\varphi}{2}\end{pmatrix}+\left(\frac{\rho}{R}\right)\begin{pmatrix}0\\0\\0\\-\frac{423\lambda^2+1222\lambda\mu+767\mu^2}{180(\lambda+\mu)^2}\sin\frac{\varphi}{2}-\frac{3\lambda+\mu}{2(\lambda+\mu)}\sin\frac{3\varphi}{2}-\frac{1}{2}\sin\frac{5\varphi}{2}\\0\\\frac{-3\lambda^2+34\lambda\mu+5\mu^2}{180(\lambda+\mu)^2}\cos\frac{\varphi}{2}+\frac{-\lambda+\mu}{2(\lambda+\mu)}\cos\frac{3\varphi}{2}-\frac{1}{2}\cos\frac{5\varphi}{2}\end{pmatrix}+\cdots\right]$$

$$+\frac{K''_{II}(\theta)}{\sqrt{2\pi\rho}}\left(\frac{\rho}{R}\right)^2\begin{pmatrix}\frac{-3\lambda+5\mu}{18(\lambda+\mu)}\sin\frac{\varphi}{2}\frac{69\lambda+77\mu}{126(\lambda+\mu)}\sin\frac{3\varphi}{2}\\\frac{2(3\lambda+2\mu)}{3(\lambda+\mu)}\sin\frac{\varphi}{2}-\frac{4\lambda(3\lambda+7\mu)}{63(\lambda+\mu)^2}\sin\frac{3\varphi}{2}\\\frac{3\lambda-5\mu}{18(\lambda+\mu)}\sin\frac{\varphi}{2}+\frac{3\lambda-5\mu}{18(\lambda+\mu)}\sin\frac{3\varphi}{2}\\0\\\frac{3\lambda+11\mu}{18(\lambda+\mu)}\cos\frac{\varphi}{2}-\frac{15\lambda+7\mu}{42(\lambda+\mu)}\cos\frac{3\varphi}{2}\\0\end{pmatrix}+\cdots$$

$$+\frac{K_{III}(\theta)}{\sqrt{2\pi\rho}}\left[\begin{pmatrix}0\\0\\0\\\frac{1}{2}\sin\frac{\varphi}{2}\\0\\\frac{1}{2}\cos\frac{\varphi}{2}\end{pmatrix}+\left(\frac{\rho}{R}\right)\begin{pmatrix}0\\0\\0\\\frac{7}{8}\sin\frac{\varphi}{2}-\frac{1}{2}\sin\frac{3\varphi}{2}\\0\\\frac{5}{8}\cos\frac{\varphi}{2}-\frac{1}{2}\cos\frac{3\varphi}{2}\end{pmatrix}+\left(\frac{\rho}{R}\right)^2\begin{pmatrix}0\\0\\0\\\frac{5}{4}\sin\frac{\varphi}{2}-\frac{39}{64}\sin\frac{3\varphi}{2}+\frac{1}{4}\sin\frac{5\varphi}{2}\\0\\\frac{1}{4}\cos\frac{\varphi}{2}-\frac{33}{64}\cos\frac{3\varphi}{2}+\frac{1}{4}\cos\frac{5\varphi}{2}\end{pmatrix}+\cdots\right]$$

$$+\frac{K'_{III}(\theta)}{\sqrt{2\pi\rho}}\left(\frac{\rho}{R}\right)\left[\begin{pmatrix}\frac{\lambda}{\mu}\sin\frac{\varphi}{2}-\frac{5\lambda+2\mu}{5\mu}\sin\frac{\varphi}{2}\\-\frac{\lambda(5\lambda+\mu)}{5\mu(\lambda+\mu)}\sin\frac{\varphi}{2}+\frac{(\lambda+2\mu)}{\mu}\sin\frac{\varphi}{2}\\0\\0\\-\frac{1}{5}\cos\frac{\varphi}{2}\\0\end{pmatrix}+\left(\frac{\rho}{R}\right)\begin{pmatrix}-\frac{39\lambda+35\mu}{30(\lambda+\mu)}\sin\frac{\varphi}{2}+\frac{2(66\lambda+53\mu)}{105(\lambda+\mu)}\sin\frac{3\varphi}{2}\\\frac{21\lambda+19\mu}{10(\lambda+\mu)}\sin\frac{\varphi}{2}-\frac{(11\lambda+7\mu)(15\lambda+13\mu)}{105(\lambda+\mu)^2}\sin\frac{3\varphi}{2}\\-\frac{3\lambda+5\mu}{15(\lambda+\mu)}\sin\frac{\varphi}{2}-\frac{3\lambda+5\mu}{15(\lambda+\mu)}\sin\frac{3\varphi}{2}\\0\\-\frac{27\lambda+19\mu}{60(\lambda+\mu)}\cos\frac{\varphi}{2}+\frac{51\lambda+47\mu}{70(\lambda+\mu)}\cos\frac{3\varphi}{2}\\0\end{pmatrix}+\cdots\right]$$

$$+\frac{K''_{III}(\theta)}{\sqrt{2\pi\rho}}\left(\frac{\rho}{R}\right)^2\begin{pmatrix}0\\0\\0\\-\frac{69\lambda+53\mu}{60(\lambda+\mu)}\sin\frac{\varphi}{2}\\0\\-\frac{9\lambda+25\mu}{60(\lambda+\mu)}\cos\frac{\varphi}{2}\end{pmatrix}+\cdots$$

Of particularly interest are the edge stress intensity functions (ESIFs) $K_I(\theta), K_{II}(\theta), K_{III}(\theta)$. To extract them we extend the QDFM derived for the Laplace equation in [17] to the elasticity system.

The mathematical derivation of the QDFM is sketched as follows. We multiply the equilibrium equations by a test function $\boldsymbol{K}(\rho,\varphi,\theta)$, (this is an arbitrary function that will have to satisfy the equilibrium equation) then integrate the equations within the torus denoted by Ω^* in Fig 1 (note that Ω^* is a 3-D domain whose cross section is shown in the figure). Finally we apply Green's theorem to obtain:

$$0=\int_{\partial\Omega^*}(\boldsymbol{K}\cdot([T]\boldsymbol{u})-([T]\boldsymbol{K})\cdot\boldsymbol{u})\,d\Gamma+\int_{\Omega^*}\boldsymbol{K}\cdot(\underbrace{\operatorname{div}\underset{\approx}{\boldsymbol{\sigma}}^{(\boldsymbol{u})}}_{0})d\Omega^*-\int_{\Omega^*}\left(\operatorname{div}\underset{\approx}{\boldsymbol{\sigma}}^{(\boldsymbol{K})}\right)\cdot\boldsymbol{u}d\Omega \tag{3}$$

where $\partial\Omega^*$ is the torus's 2-D surface, $[T]\boldsymbol{u}$ and $[T]\boldsymbol{K}$ are the tractions on Γ associated with $\boldsymbol{u}$ and the test vector $\boldsymbol{K}$:

$$[T]\boldsymbol{u} = \left(\sigma_{\rho\rho}^{(\boldsymbol{u})}, \sigma_{\rho\varphi}^{(\boldsymbol{u})}, \sigma_{\rho\theta}^{(\boldsymbol{u})}\right)^T, \quad [T]\boldsymbol{K} = \left(\sigma_{\rho\rho}^{(\boldsymbol{K})}, \sigma_{\rho\varphi}^{(\boldsymbol{K})}, \sigma_{\rho\theta}^{(\boldsymbol{K})}\right)^T \tag{4}$$

and $\sigma^{(\boldsymbol{u})}$ and $\sigma^{(\boldsymbol{K})}$ denote the stresses associated with either the displacement field $\boldsymbol{u}$ or $\boldsymbol{K}$ using (B.1).

Formally, the expansion (1) is the solution to the elasticity system whether α_k is positive or negative. However, the negative eigenvalues (and the corresponding dual eigenfunctions and shadows) result in an infinite displacement at the crack edge, so are inadmissible from the "physical" viewpoint (and from the mathematical viewpoint because the solution should lie in the space H^1). Nevertheless, we may construct using these negative eigenvalues and the corresponding dual eigenfunctions and shadows a test function $\boldsymbol{K}$. This way, $\boldsymbol{K}$ also satisfies identically the equilibrium equation which is written in a condensed manner $\operatorname{div} \underset{\approx}{\boldsymbol{\sigma}}^{(\boldsymbol{K})} = \boldsymbol{0}$. Of course we cannot construct $\boldsymbol{K}$ by a dual eigenpair and its infinite number of shadows, so we define the **quasi-dual function** $\boldsymbol{K}_{n,m}^{(\alpha_j)}(\rho,\varphi,\theta)$ that is based on one dual eigenfunction $\boldsymbol{\psi}_{0,j,0}(\varphi)$ and a **finite** series of dual shadows $\boldsymbol{\psi}_{h,j,f}(\varphi)$:

$$\boldsymbol{K}_{n,m}^{(\alpha_j)} \overset{\text{def}}{=} \sum_{h=0,1,2,\cdots}^{m} \partial_\theta^h B_j(\theta)\rho^{-\alpha_j} \sum_{f=0}^{n} \left(\frac{\rho}{R}\right)^{h+f} \boldsymbol{\psi}_{h,j,f}(\varphi) \tag{5}$$

$B_j(\theta)$ in an arbitrarily chosen function to be specified in the sequel. The explicit recursive equations for the determination of $\boldsymbol{\psi}_{h,j,f}(\varphi)$ are provided in Appendix A.

Remark 1. *Because the Navier-Lamé system (the elasticity system) without body forces is nothing more than* $\operatorname{div} \underset{\approx}{\boldsymbol{\sigma}}^{(\boldsymbol{u})} = 0$, *then* $\operatorname{div} \underset{\approx}{\boldsymbol{\sigma}}^{\left(\boldsymbol{K}_{n,m}^{(\alpha_j)}\right)}$ *is zero only for* $n,m \to \infty$. *For* ***finite*** n *and* m, $\operatorname{div} \underset{\approx}{\boldsymbol{\sigma}}^{\left(\boldsymbol{K}_{n,m}^{(\alpha_j)}\right)} \neq 0$, *thus the last term in* (3) *is not zero.*

On the two flat surfaces Γ_1 and Γ_2 (faces that intersect at the crack edge) traction free boundary conditions are considered, i.e. $\sigma_{\rho\rho}^{(\boldsymbol{u})} = \sigma_{\rho\varphi}^{(\boldsymbol{u})} = \sigma_{\rho\theta}^{(\boldsymbol{u})} = 0$ and $\sigma_{\rho\rho}^{(\boldsymbol{K})} = \sigma_{\rho\varphi}^{(\boldsymbol{K})} = \sigma_{\rho\theta}^{(\boldsymbol{K})} = 0$, thus (3) reduces to (note that on the crack surfaces either $[T]\boldsymbol{u} = \boldsymbol{0}$ because of the traction-free condition on crack surfaces, or $[T]\boldsymbol{K} = \boldsymbol{0}$ since the $\boldsymbol{K}$ is constructed using the dual solutions):

$$\begin{aligned} &\int_0^{2\pi}\int_{\varphi_1}^{\varphi_2} (\boldsymbol{K}_{n,m}^{(\alpha_j)} \cdot [T]\boldsymbol{u} - [T]\boldsymbol{K}_{n,m}^{(\alpha_j)} \cdot \boldsymbol{u})\big|_{\rho_0} (R+\rho_0\cos\varphi)\rho_0 d\varphi d\theta \qquad (6)\\ = &\int_0^{2\pi}\int_{\varphi_1}^{\varphi_2} (\boldsymbol{K}_{n,m}^{(\alpha_j)}[T] \cdot \boldsymbol{u} - [T]\boldsymbol{K}_{n,m}^{(\alpha_j)} \cdot \boldsymbol{u})\big|_{\rho_1} (R+\rho_1\cos\varphi)\rho_1 d\varphi d\theta + \int_{\Omega^*} \operatorname{div} \underset{\approx}{\boldsymbol{\sigma}}^{\boldsymbol{K}_{n,m}^{(\alpha_j)}} \cdot \boldsymbol{u}\, d\Omega\,. \end{aligned}$$

Definition 1. *We define the surface-integral* $Q_\rho[\boldsymbol{u}, \boldsymbol{K}_{n,m}^{(\alpha_j)}]$ *over the torus of minor*

radius ρ *and major radius* R *that surrounds the circular edge:*

$$\boxed{Q_\rho\left[\boldsymbol{u},\boldsymbol{K}_{n,m}^{(\alpha_j)}\right]\overset{\text{def}}{=}\int_0^{2\pi}\int_{\varphi_1}^{\varphi_2}\left(\boldsymbol{K}_{n,m}^{(\alpha_j)}\cdot[T]\boldsymbol{u}-[T]\boldsymbol{K}_{n,m}^{(\alpha_j)}\cdot\boldsymbol{u}\right)_\rho(R+\rho\cos\varphi)\rho\,d\varphi d\theta.} \tag{7}$$

Remark 2. *In our previous publications we used the notation of* J_ρ *, however this notation is easily confused with the J-integral which is completely different so we changed the notation to* Q_ρ *to reduce any confusion.*

With this notation, (6) may be restated as:

$$Q_{\rho_0}\left[\boldsymbol{u},\boldsymbol{K}_{n,m}^{(\alpha_j)}\right]=Q_{\rho_1}\left[\boldsymbol{u},\boldsymbol{K}_{n,m}^{(\alpha_j)}\right]+\int_{\Omega^*}\text{div}\underset{\approx}{\boldsymbol{\sigma}}^{\boldsymbol{K}_{n,m}^{(\alpha_j)}}\cdot\boldsymbol{u}\,d\Omega. \tag{8}$$

By substituting (5) in the equilibrium equation one obtains:

$$\begin{aligned}\text{div}\underset{\approx}{\boldsymbol{\sigma}}^{\boldsymbol{K}_{n,m}^{(\alpha_j)}} &= \mathcal{O}\left\{\rho^{-\alpha_j-2}\left[B_j(\theta)\left(\frac{\rho}{R}\right)^{n+1}+\partial_\theta^{m+1}B_j(\theta)\left(\frac{\rho}{R}\right)^{m+1}\right]\right\} \quad (9)\\ &= \mathcal{O}\left\{\rho^{-\alpha_j-2}\left(\frac{\rho}{R}\right)^{1+min(n,m)}\right\}\end{aligned}$$

Multiplying (9) by (1) and integrating over Ω^* with $d\Omega=R\rho\left(1+\frac{\rho}{R}\cos\varphi\right)d\rho d\varphi d\theta$:

$$\int_{\Omega^*}\text{div}\underset{\approx}{\boldsymbol{\sigma}}^{\boldsymbol{K}_{n,m}^{(\alpha_j)}}\cdot\boldsymbol{u}d\Omega=\mathcal{O}\left\{\rho^{\alpha_0-\alpha_j}\left(\frac{\rho}{R}\right)^{1+min(n,m)}\right\}\Big|_{\rho_1}^{\rho_0} \tag{10}$$

Substituting (10) in (8) one observes that in contrast to the 2-D case, $Q_\rho\left[\boldsymbol{u},\boldsymbol{K}_{n,m}^{(\alpha_j)}\right]$ is surface-dependent:

$$Q_{\rho_0}\left[\boldsymbol{u},\boldsymbol{K}_{n,m}^{(\alpha_j)}\right]=Q_{\rho_1}\left[\boldsymbol{u},\boldsymbol{K}_{n,m}^{(\alpha_j)}\right]+\mathcal{O}\left\{\rho^{\alpha_0-\alpha_j}\left(\frac{\rho}{R}\right)^{1+min(n,m)}\right\}\Big|_{\rho_1}^{\rho_0} \tag{11}$$

Remark 3. *The choice* $m=n$ *optimizes the number of shadow functions with respect to* m *and* n *, and furthermore we take the limit as* $\rho_1\to 0$ *then* (11) *becomes*

$$Q_{\rho_0}\left[\boldsymbol{u},\boldsymbol{K}_{n,n}^{(\alpha_j)}\right]=Q_{\rho_1}\left[\boldsymbol{u},\boldsymbol{K}_{n,n}^{(\alpha_j)}\right]+\mathcal{O}\left(\rho_0^{\alpha_0-\alpha_j}\left(\frac{\rho_0}{R}\right)^{1+n}\right) \tag{12}$$

Evaluating $Q_{\rho_1}\left[\boldsymbol{u},\boldsymbol{K}_{n,n}^{(\alpha_j)}\right]$ as $\rho_1\to 0$ one notices that $[T]\boldsymbol{K}_{n,n}^{(\alpha_j)}$ and $[T]\boldsymbol{u}$ tend to infinity whereas $\boldsymbol{u}$ and ρ_1 tend to zero. Since the left hand side of (12) is evaluated at a finite ρ_0 then $Q_{\rho_1}\left[\boldsymbol{u},\boldsymbol{K}_{n,n}^{(\alpha_j)}\right]$ has to go at the limit $\rho_1\to 0$ to a given limit which is a constant. This implies that:

$$\boxed{Q_{\rho_0}\left[\boldsymbol{u},\boldsymbol{K}_{n,n}^{(\alpha_j)}\right]=Const+\mathcal{O}\left(\rho_0^{\alpha_0-\alpha_j}\left(\frac{\rho_0}{R}\right)^{1+n}\right)} \tag{13}$$

Finally we conclude that $Q_\rho\left[\boldsymbol{u},\boldsymbol{K}_{n,n}^{(\alpha_j)}\right]$ is pseudo-path-independent, i.e. the difference in the integral value between two paths tends to zero as the number of shadow functions n is increased, or the ratio ρ/R decreases.

One notices that the integral $Q_{\rho_0}[\boldsymbol{u},\boldsymbol{K}_{n,m}^{(\alpha_j)}]$ over a torus of minor radius ρ_0 and major radius R that surrounds the circular edge is mildly path dependent, with such a dependency vanishing as $\rho_0\to 0$ and $n\to\infty$.

3. Connecting the path integral $\boldsymbol{Q_\rho\left[u,K_{n,n}^{(\alpha_j)}\right]}$ and an ESIF - The axisymmetric case

Consider first for simplicity the **axisymmetric** case (A_k s are θ independent), for which the solution $\boldsymbol{u}$ in (1) is simplified to $(\ell=0)$:

$$\boldsymbol{u}(\rho,\varphi)=\sum_{k=0}A_k\rho^{\alpha_k}\sum_{i=0}^{\infty}\left(\frac{\rho}{R}\right)^i\boldsymbol{\phi}_{0,k,i}(\varphi) \tag{14}$$

In this case $\boldsymbol{K}_{n,0}^{(\alpha_j)}$ coincides with $\boldsymbol{K}_{n,n}^{(\alpha_j)}$ for any n. For extracting A_j we compute $Q_\rho[\boldsymbol{u},\boldsymbol{K}_{n,0}^{(\alpha_j)}]$ by (5), and then take $\rho\to 0$, with B_j being θ independent, and we chose the QDF $\boldsymbol{K}_{n,0}^{(\alpha_j)}$ in (7) for the axisymmetric case ($m=0$):

$$\boldsymbol{K}_{n,0}^{(\alpha_j)}(\rho,\varphi)\triangleq B_j\rho^{-\alpha_j}\sum_{i=0}^{n}\left(\frac{\rho}{R}\right)^i\boldsymbol{\psi}_{0,j,i}(\varphi) \tag{15}$$

Because there is no θ-dependency, the integration over θ results in 2π and $Q_\rho[\boldsymbol{u},\boldsymbol{K}_{n,0}^{(\alpha_j)}]$ reduces to:

$$Q_\rho\left[\boldsymbol{u},\boldsymbol{K}_{n,0}^{(\alpha_j)}\right]\overset{\text{def}}{=}2\pi\int_{\varphi_1}^{\varphi_2}\left\{\boldsymbol{K}_{n,0}^{(\alpha_j)}\cdot[T]\boldsymbol{u}-[T]\boldsymbol{K}_{n,0}^{(\alpha_j)}\cdot\boldsymbol{u}\right\}_\rho R\left(1+\frac{\rho}{R}\cos\varphi\right)\rho d\varphi \tag{16}$$

Inserting (14) in (16) one obtains

$$Q_\rho\left[\boldsymbol{u},\boldsymbol{K}_{n,0}^{(\alpha_j)}\right]\overset{\rho\to 0}{=}\begin{cases}\frac{32\pi^2\alpha_j\mu(\lambda+2\mu)R}{\left(\alpha_j^2-1\right)(\lambda+\mu)}A_jB_j & j=1,2,7,8,13,14\cdots\\ 4\pi^2\alpha_j\mu RA_jB_j & j=3,9,15\end{cases} \tag{17}$$

Remark 4. *The ESIFs associated with the integer eigenvalues are not addressed here.*

Thus we choose:

$$B_j=\frac{\left(\alpha_j^2-1\right)(\lambda+\mu)}{32\pi^2\alpha_j\mu(\lambda+2\mu)R},\qquad j=1,2,7,8,13,14\cdots \tag{18}$$

$$B_j=\frac{1}{4\pi^2\alpha_j\mu R},\qquad j=3,9,15\cdots \tag{19}$$

Remark 5. *To extract the ESIFs associated with mode I and mode II* $(i.e.\ A_1,A_2,A_7,A_8,A_{13},A_{14}\cdots)$, *we choose* B_j *according to* (18)*, whereas for the ESIFs associated with mode III* $(i.e.\ A_3,A_9,A_{15}\cdots)$, *we choose* B_j *according to* (19)*.*

Remark 6. *For example, for a circular crack with traction-free BCs,* B_1 *is:*

$$B_1 = -\frac{3(\lambda+\mu)}{64\pi^2\mu R(\lambda+2\mu)} \tag{20}$$

In conclusion, using $Q_{\rho_0}\left[\boldsymbol{u}, \boldsymbol{K}_{n,0}^{(\alpha_j)}\right]$ with the *extraction constant* given by either (18) or (19) one obtains the required ESIF:

$$\boxed{Q_{\rho_0}\left[\boldsymbol{u}, \boldsymbol{K}_{n,0}^{(\alpha_j)}\right] = A_j + \mathcal{O}\left(\rho_0^{\alpha_0-\alpha_j}\left(\frac{\rho_o}{R}\right)^{n+1}\right)} \tag{21}$$

3.1. A penny-shaped crack with traction-free BCs

For a penny-shaped crack with homogenous Neumann BCs, $\omega = 2\pi$, $(\varphi_1 = -\pi, \varphi_2 = \pi)$ the eigenvalues are $\alpha_j = 0,0,0,\frac{1}{2},\frac{1}{2},\frac{1}{2},1,1,1,\frac{3}{2},\frac{3}{2},\frac{3}{2},2,2,2,\cdots$.

The solution $\boldsymbol{u}$ in the vicinity of the crack front is (see [22] with the explicit expressions for $\boldsymbol{\phi}_{0,k,i}$ provided in [16]):

$$\begin{aligned}
\boldsymbol{u} \;=\; & A_{0_1}\sum_{i=0}^{5}\left(\frac{\rho}{R}\right)^i\boldsymbol{\phi}_{0,0_1,i} + A_{0_2}\boldsymbol{\phi}_{0,0_2,0} + A_{0_3}\sum_{i=0}^{1}\left(\frac{\rho}{R}\right)^i\boldsymbol{\phi}_{0,0_3,i} \\
& + A_1\rho^{1/2}\sum_{i=0}^{4}\left(\frac{\rho}{R}\right)^i\boldsymbol{\phi}_{0,1,i} + A_2\rho^{1/2}\sum_{i=0}^{4}\left(\frac{\rho}{R}\right)^i\boldsymbol{\phi}_{0,2,i} + A_3\rho^{1/2}\sum_{i=0}^{4}\left(\frac{\rho}{R}\right)^i\boldsymbol{\phi}_{0,3,i} \\
& + A_4\rho\sum_{i=0}^{4}\left(\frac{\rho}{R}\right)^i\boldsymbol{\phi}_{0,4,i} + A_5\rho\sum_{i=0}^{4}\left(\frac{\rho}{R}\right)^i\boldsymbol{\phi}_{0,5,i} + A_6\rho\sum_{i=0}^{4}\left(\frac{\rho}{R}\right)^i\boldsymbol{\phi}_{0,6,i} \\
& + A_7\rho^{3/2}\sum_{i=0}^{3}\left(\frac{\rho}{R}\right)^i\boldsymbol{\phi}_{0,7,i} + A_8\rho^{3/2}\sum_{i=0}^{3}\left(\frac{\rho}{R}\right)^i\boldsymbol{\phi}_{0,8,i} + A_9\rho^{3/2}\sum_{i=0}^{3}\left(\frac{\rho}{R}\right)^i\boldsymbol{\phi}_{0,9,i} + \cdots
\end{aligned} \tag{22}$$

Extracting A_1

To extract A_1 , the extraction function B_1 in (20) is used and we construct the QDF $\boldsymbol{K}_{0,0}^{(\alpha_1=1/2)}, \ldots, \boldsymbol{K}_{3,0}^{(1/2)}$. For example the QDF $\boldsymbol{K}_{3,0}^{(1/2)}$ is:

$$\begin{aligned}
K_{3,0}^{(1/2)} \;=\; & B_1\rho^{-1/2}\left\{\begin{pmatrix} \cos\frac{\varphi}{2} - \frac{(3\lambda+7\mu)}{3(\lambda+\mu)}\cos\frac{3\varphi}{2} \\ -\sin\frac{\varphi}{2} + \frac{(\lambda+5\mu)}{3(\lambda+\mu)}\sin\frac{3\varphi}{2} \\ 0\end{pmatrix} + \left(\frac{\rho}{R}\right)\begin{pmatrix} -\frac{\left(\lambda^2-14\lambda\mu-47\mu^2\right)}{12(\lambda+\mu)^2}\cos\frac{\varphi}{2} + \frac{\lambda+5\mu}{12(\lambda+\mu)}\cos\frac{5\varphi}{2} \\ -\frac{\left(5\lambda^2+42\lambda\mu+69\mu^2\right)}{12(\lambda+\mu)^2}\sin\frac{\varphi}{2} - \frac{-\lambda+3\mu}{12(\lambda+\mu)}\sin\frac{5\varphi}{2} \\ 0\end{pmatrix}\right. \\
& + \left(\frac{\rho}{R}\right)^2\begin{pmatrix} -\frac{4(3\lambda-\mu)\mu(\lambda+2\mu)}{9(\lambda+\mu)^3}\cos\frac{\varphi}{2} - \frac{(\lambda+9\mu)(3\lambda+11\mu)}{96(\lambda+\mu)^2}\cos\frac{3\varphi}{2} + \frac{(\lambda-3\mu)}{32(\lambda+\mu)}\cos\frac{7\varphi}{2} \\ \frac{4\mu(\lambda+2\mu)(3\lambda+7\mu)}{9(\lambda+\mu)^3}\sin\frac{\varphi}{2} + \frac{\left(21\lambda^2+106\lambda\mu+149\mu^2\right)}{96(\lambda+\mu)^2}\sin\frac{3\varphi}{2} + \frac{(-3\lambda+\mu)}{32(\lambda+\mu)}\sin\frac{7\varphi}{2} \\ 0\end{pmatrix} \\
& \left. + \left(\frac{\rho}{R}\right)^3\begin{pmatrix} \frac{\mu(\lambda+2\mu)(9\lambda+5\mu)}{9(\lambda+\mu)^3}\cos\frac{\varphi}{2} + \frac{2\mu(\lambda+2\mu)\left(45\lambda^2+42\lambda\mu+13\mu^2\right)}{135(\lambda+\mu)^4}\cos\frac{3\varphi}{2} + \frac{5\lambda^2+26\lambda\mu+53\mu^2}{128(\lambda+\mu)^2}\cos\frac{5\varphi}{2} - \frac{5(3\lambda-\mu)}{384(\lambda+\mu)}\cos\frac{9\varphi}{2} \\ -\frac{(3\lambda-\mu)\mu(\lambda+2\mu)}{9(\lambda+\mu)^3}\sin\frac{\varphi}{2} - \frac{2\mu(\lambda+2\mu)\left(45\lambda^2+98\lambda\mu+37\mu^2\right)}{135(\lambda+\mu)^4}\sin\frac{3\varphi}{2} + \frac{-15\lambda^2-62\lambda\mu-79\mu^2}{128(\lambda+\mu)^2}\sin\frac{5\varphi}{2} + \frac{5(5\lambda+\mu)}{384(\lambda+\mu)}\sin\frac{9\varphi}{2} \\ 0\end{pmatrix}\right\}
\end{aligned} \tag{23}$$

We substitute (22) and $K_{0,0}^{(1/2)},\ldots,K_{3,0}^{(1/2)}$ in (16) with $\lambda=15/26$, $\mu=5/13$, $(E=1,\ \nu=0.3)$ to obtain:

$$Q_\rho\left[\boldsymbol{u},\boldsymbol{K}_{0,0}^{(1/2)}\right] = \left(1-\frac{5\rho}{64R}+\cdots\right)A_1+\left(-\frac{43\rho^{3/2}}{900\pi R}+\cdots\right)A_4+\left(-\frac{5\rho^2}{32R}+\cdots\right)A_7 + \left(\frac{\sqrt{\rho}}{84\pi R}+\cdots\right)A_{0_1}=A_1+\mathcal{O}\left(\frac{\rho^{1/2}}{R}\right)A_{0_1} \tag{24}$$

$$Q_\rho\left[\boldsymbol{u},\boldsymbol{K}_{1,0}^{(1/2)}\right] = \left(1-\frac{547\rho^2}{1280R^2}+\cdots\right)A_1+\left(-\frac{2363\rho^{5/2}}{462000\pi R^2}+\cdots\right)A_4+\left(-\frac{\rho^3}{4R^2}+\cdots\right)A_7 + \left(\frac{7\rho^{3/2}}{16\pi R^2}+\cdots\right)A_{0_1}=A_1+\mathcal{O}\left(\frac{\rho^{3/2}}{R^2}\right)A_{0_1} \tag{25}$$

$$Q_\rho\left[\boldsymbol{u},\boldsymbol{K}_{2,0}^{(1/2)}\right] = \left(1+\frac{3889\rho^3}{6000R^3}+\cdots\right)A_1+\left(-\frac{505523\rho^{7/2}}{1456000\pi R^3}+\cdots\right)A_4+\left(\frac{12219\rho^4}{51200R^3}+\cdots\right)A_7 + \left(-\frac{2904791\rho^{5/2}}{3696000\pi R^3}+\cdots\right)A_{0_1}=A_1+\mathcal{O}\left(\frac{\rho^{5/2}}{R^3}\right)A_{0_1} \tag{26}$$

$$Q_\rho\left[\boldsymbol{u},\boldsymbol{K}_{3,0}^{(1/2)}\right] = \left(1-\frac{91241\rho^4}{144000R^4}+\cdots\right)A_1+\left(\frac{1488670331\rho^{9/2}}{1995840000\pi R^4}+\cdots\right)A_4 + \left(\frac{74453573\rho^5}{230400000R^4}+\cdots\right)A_7+\left(\frac{27209149\rho^{7/2}}{22464000\pi R^4}+\cdots\right)A_{0_1}=A_1+\mathcal{O}\left(\frac{\rho^{7/2}}{R^4}\right)A_{0_1} \tag{27}$$

Observing (24)-(27) one notices that:

$$Q_\rho\left[\boldsymbol{u},\boldsymbol{K}_{n,0}^{(\alpha_1=1/2)}\right]=A_1+\mathcal{O}\left(\rho^{-1/2}\left(\frac{\rho}{R}\right)^{n+1}\right) \tag{28}$$

This is exactly the expected result since $\alpha_0-\alpha_1=-1/2$.

Extracting A_2

We compute $Q_{\rho_0}[\boldsymbol{u},\boldsymbol{K}_{n,0}^{(\alpha_2=1/2)}]$, for $\alpha_2=1/2$, with $B_2=B_1=-\frac{3(\lambda+\mu)}{64\pi^2R\mu(\lambda+2\mu)}$.

For example, for $n=3$ the QDF $\boldsymbol{K}_{3,0}^{(1/2)}$ is:

$$
\begin{aligned}
\boldsymbol{K}_{3,0}^{(1/2)} &= B_2\rho^{-1/2}\left[\begin{pmatrix} \sin\frac{\varphi}{2}-\frac{(3\lambda+7\mu)}{\lambda+\mu}\sin\frac{3\varphi}{2} \\ \cos\frac{\varphi}{2}-\frac{(\lambda+5\mu)}{\lambda+\mu}\cos\frac{3\varphi}{2} \\ 0\end{pmatrix}+\left(\frac{\rho}{R}\right)\begin{pmatrix} \frac{25\lambda^2+34\lambda\mu-23\mu^2}{12(\lambda+\mu)^2}\sin\frac{\varphi}{2}+\frac{(\lambda+5\mu)}{4(\lambda+\mu)}\sin\frac{5\varphi}{2} \\ \frac{3\lambda^2-26\lambda\mu-61\mu^2}{12(\lambda+\mu)^2}\cos\frac{\varphi}{2}-\frac{(\lambda-3\mu)}{4(\lambda+\mu)}\cos\frac{5\varphi}{2} \\ 0\end{pmatrix}\right. \\
&+ \left(\frac{\rho}{R}\right)^2\begin{pmatrix} \frac{4(\lambda+2\mu)\left(15\lambda^2+19\lambda\mu+8\mu^2\right)}{45(\lambda+\mu)^3}\sin\frac{\varphi}{2}-\frac{205\lambda^2+506\lambda\mu+237\mu^2}{96(\lambda+\mu)^2}\sin\frac{3\varphi}{2}+\frac{3(\lambda-3\mu)}{32(\lambda+\mu)}\sin\frac{7\varphi}{2} \\ \frac{4\left(15\lambda^3+65\lambda^2\mu+86\lambda\mu^2+32\mu^3\right)}{45(\lambda+\mu)^3}\cos\frac{\varphi}{2}-\frac{155\lambda^2+374\lambda\mu+155\mu^2}{96(\lambda+\mu)^2}\cos\frac{3\varphi}{2}+\frac{3(3\lambda-\mu)}{32(\lambda+\mu)}\cos\frac{7\varphi}{2} \\ 0\end{pmatrix} \\
&+ \left(\frac{\rho}{R}\right)^3\left.\begin{pmatrix} \frac{(\lambda+2\mu)\left(75\lambda^2+117\lambda\mu+46\mu^2\right)}{45(\lambda+\mu)^3}\sin\frac{\varphi}{2}-\frac{2(\lambda+2\mu)\left(525\lambda^3+1070\lambda^2\mu+709\lambda\mu^2+148\mu^3\right)}{1575(\lambda+\mu)^4}\sin\frac{3\varphi}{2} \\ -\frac{(\lambda+2\mu)\left(15\lambda^2+57\lambda\mu+38\mu^2\right)}{45(\lambda+\mu)^3}\cos\frac{\varphi}{2}-\frac{2\lambda+2\mu)\left(525\lambda^3+1470\lambda^2\mu+1261\lambda\mu^2+332\mu^3\right)}{1575(\lambda+\mu)^4}\cos\frac{3\varphi}{2} \\ 0\end{pmatrix}\right] \\
&\qquad\qquad \begin{pmatrix} +\frac{179\lambda^2+470\lambda\mu+259\mu^2}{128(\lambda+\mu)^2}\sin\frac{5\varphi}{2}-\frac{5(3\lambda-\mu)}{128(\lambda+\mu)}\sin\frac{9\varphi}{2} \\ +\frac{153\lambda^2+402\lambda\mu+217\mu^2}{128(\lambda+\mu)^2}\cos\frac{5\varphi}{2}-\frac{5(5\lambda+\mu)}{128(\lambda+\mu)}\cos\frac{9\varphi}{2} \\ 0\end{pmatrix}\Bigg] \qquad (29)
\end{aligned}
$$

A_2 is computed by substituting (22) and $K_{0,0}^{(1/2)},\ldots,K_{3,0}^{(1/2)}$ in (16) with $\lambda = 15/26,\ \mu = 5/13,\ (E=1,\ \nu=0.3)$:

$$
\begin{aligned}
Q_\rho\left[\boldsymbol{u},\boldsymbol{K}_{0,0}^{(1/2)}\right] &= \left(1+\frac{15\rho}{64R}+\cdots\right)A_2+\left(-\frac{14\rho^{3/2}}{13\pi R}+\cdots\right)A_5+\left(\frac{33\rho^2}{160R}+\cdots\right)A_8 \\
&\quad -\frac{11\sqrt{\rho}}{14\pi R}A_{0_2} = A_2+\mathcal{O}\left(\frac{\rho^{1/2}}{R}\right)A_{0_2} \qquad (30)
\end{aligned}
$$

$$
\begin{aligned}
Q_\rho\left[\boldsymbol{u},\boldsymbol{K}_{1,0}^{(1/2)}\right] &= \left(1+\frac{1763\rho^2}{1280R^2}+\cdots\right)A_2+\left(-\frac{913\rho^{5/2}}{390\pi R^2}+\cdots\right)A_5+\left(\frac{7\rho^3}{40R^2}+\cdots\right)A_8 \\
&\quad +\frac{61\rho^{3/2}}{120\pi R^2}A_{0_2} = A_2+\mathcal{O}\left(\frac{\rho^{3/2}}{R^2}\right)A_{0_2} \qquad (31)
\end{aligned}
$$

$$
\begin{aligned}
Q_\rho\left[\boldsymbol{u},\boldsymbol{K}_{2,0}^{(1/2)}\right] &= \left(1+\frac{230167\rho^3}{180000R^3}+\cdots\right)A_2+\left(-\frac{19807\rho^{7/2}}{15600\pi R^3}+\cdots\right)A_5 \qquad (32) \\
&\quad +\left(-\frac{666699\rho^4}{1280000R^3}+\cdots\right)A_8-\frac{19527433\rho^{5/2}}{9240000\pi R^3}A_{0_2} = A_2+\mathcal{O}\left(\frac{\rho^{5/2}}{R^3}\right)A_{0_2}
\end{aligned}
$$

$$
\begin{aligned}
Q_\rho\left[\boldsymbol{u},\boldsymbol{K}_{3,0}^{(1/2)}\right] &= \left(1+\frac{4071269\rho^4}{1440000R^4}+\cdots\right)A_2+\left(-\frac{521137547\rho^{9/2}}{154440000\pi R^4}+\cdots\right)A_5 \qquad (33) \\
&\quad +\left(\frac{220603473\rho^5}{640000000R^4}+\cdots\right)A_8+\frac{233573881\rho^{7/2}}{655200000\pi R^4}A_{0_2} = A_2+\mathcal{O}\left(\frac{\rho^{7/2}}{R^4}\right)A_{0_2}
\end{aligned}
$$

Again, one notices that:

$$
Q_\rho\left[\boldsymbol{u},\boldsymbol{K}_{n,0}^{(1/2)}\right] = A_2+\mathcal{O}\left(\rho^{-1/2}\left(\frac{\rho}{R}\right)^{n+1}\right) \qquad (34)
$$

Extracting A_3

For $\alpha_3 = 1/2$, $B_3 = \frac{1}{2\pi^2 R\mu}$ (see (19)). For example, for $n = 3$ the QDF $\boldsymbol{K}_{3,0}^{(\alpha_3=1/2)}$ is:

$$\begin{aligned}\boldsymbol{K}_{3,0}^{(\alpha_3=1/2)} &= B_3\rho^{-1/2}\begin{pmatrix}0\\0\\\sin\frac{\varphi}{2}\end{pmatrix} + B_3\rho^{-1/2}\left(\frac{\rho}{R}\right)\begin{pmatrix}0\\0\\-\frac{1}{4}\sin\frac{3\varphi}{2}\end{pmatrix} \\ &+B_3\rho^{-1/2}\left(\frac{\rho}{R}\right)^2\begin{pmatrix}0\\0\\\frac{1}{2}\sin\frac{\varphi}{2}+\frac{3}{32}\sin\frac{5\varphi}{2}\end{pmatrix} + B_3\rho^{-1/2}\left(\frac{\rho}{R}\right)^3\begin{pmatrix}0\\0\\\frac{1}{4}\sin\frac{\varphi}{2}-\frac{3}{8}\sin\frac{3\varphi}{2}+-\frac{5}{128}\sin\frac{7\varphi}{2}\end{pmatrix}\end{aligned} \tag{35}$$

Substituting (22) and $K_{0,0}^{(1/2)},\ldots,K_{3,0}^{(1/2)}$ in (16) with $\lambda = 15/26$, $\mu = 5/13$, $(E = 1,\ \nu = 0.3)$ one obtains:

$$Q_\rho\left[\boldsymbol{u},\boldsymbol{K}_{0,0}^{1/2}\right] = \left(1+\frac{\rho^2}{2R^2}+\cdots\right)A_3+\left(\frac{\rho^2}{4R}+\cdots\right)A_9 = A_3+\mathcal{O}\left(\frac{\rho^2}{R^2}\right)A_3, \tag{36}$$

$$Q_\rho\left[\boldsymbol{u},\boldsymbol{K}_{1,0}^{1/2}\right] = \left(1+\frac{\rho^2}{2R^2}+\cdots\right)A_3+\left(-\frac{\rho^4}{4R^3}+\cdots\right)A_9 = A_3+\mathcal{O}\left(\frac{\rho^2}{R^2}\right)A_3, \tag{37}$$

$$Q_\rho\left[\boldsymbol{u},\boldsymbol{K}_{2,0}^{1/2}\right] = \left(1+\frac{\rho^3}{2R^3}+\cdots\right)A_3+\left(-\frac{3\rho^4}{8R^3}+\cdots\right)A_9 = A_3+\mathcal{O}\left(\frac{\rho^3}{R^3}\right)A_3, \tag{38}$$

$$Q_\rho\left[\boldsymbol{u},\boldsymbol{K}_{3,0}^{1/2}\right] = \left(1+\frac{15\rho^4}{16R^4}+\cdots\right)A_3+\left(\frac{5\rho^5}{16R^4}+\cdots\right)A_9 = A_3+\mathcal{O}\left(\frac{\rho^4}{R^4}\right)A_3 \tag{39}$$

Following (36)-(39):

$$Q_\rho\left[\boldsymbol{u},\boldsymbol{K}_{n,0}^{(\alpha_3=1/2)}\right] = A_3+\mathcal{O}\left(\frac{\rho}{R}\right)^{n+1} \tag{40}$$

Remark 7. *In the case of mode III the remainder of* $Q_\rho\left[\boldsymbol{u},\boldsymbol{K}_{n,0}^{(\alpha_3=1/2)}\right]$ *is* $\left(\frac{\rho}{R}\right)^{n+1}$ *instead of* $\rho^{-1/2}\left(\frac{\rho}{R}\right)^{n+1}$ *as for mode I & II.*

Remark 8. *If a rigid body motion of the crack edge is absent (the coefficient* $A_{0i}=0$*) then the remainder when extracting* A_1 *and* A_2 *is of order* $\mathcal{O}\left(\left(\frac{\rho}{R}\right)^{n+1}\right)$*. This is* $\rho^{1/2}$ *faster compared to the case when there are rigid body motion of the crack edge present. In [17] the same is true for the Laplace equation, although this observation was not highlighted in that paper.*

As an example we consider (22) with $A_{0_1} = A_{0_2} = A_{0_3} = A_1 = A_2 = ... = 1$ and extract A_1 by the QDFM with QDFs of orders $n = 0,1,2,3$ and for different ρ_0 s for a penny-shaped crack of radius $R = 1$. The relative error as percentage of the "extracted A_1" is defined as:

$$e_{A_1}\% = 100\times\left|\frac{A_1 - A_1^{\mathsf{Exact}}}{A_1^{\mathsf{Exact}}}\right| \tag{41}$$

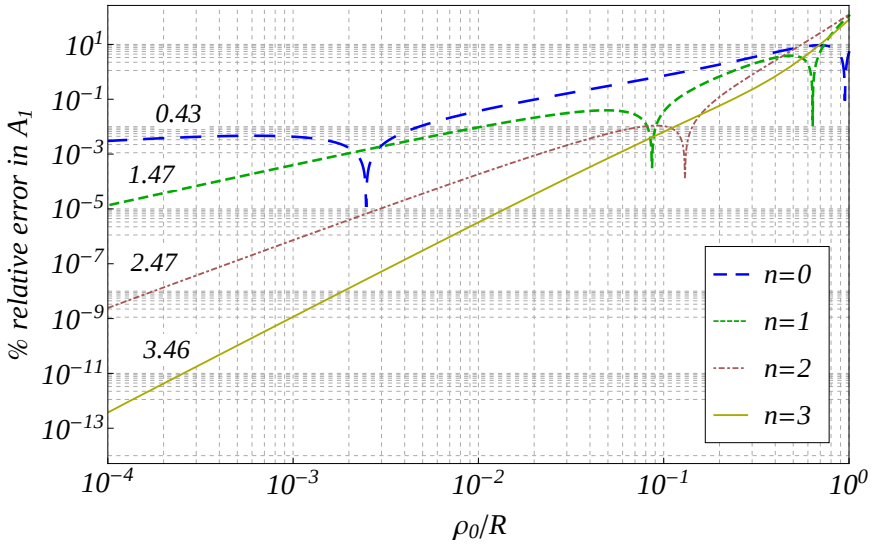

Figure 2: Convergence of the extracted A_1 with different QDFs. The numbers above the lines are the asymptotic rates of convergence that are very close to the theoretical estimates.

In Figure 2 we present the relative error of the extracted ESIF as a function of ρ_0 and n and the asymptotic rate of convergence (these are the numbers close to the left axis). Figure 2 demonstrates that the theoretical asymptotic rate of convergence is attained as $\rho_0 \to 0$, and as n increases.

3.2. Extracting ESIFs from p-FE solutions

In general the exact solution $\boldsymbol{u}$ is unknown but only a numerical approximation $\boldsymbol{u}_{\mathsf{FE}}$ is available. Thus we apply the QDFM in conjunction with the p-version of the FE method. Several 3-D FE models with a circular crack are considered. Here the finite element solution $\boldsymbol{u}_{\mathsf{FE}}$ and $\boldsymbol{\sigma}_{\mathsf{FE}}$ are extracted on a torus surface which surrounds the circular singular edge (see Figure 3), and $Q_{\rho_0}[\boldsymbol{u}_{\mathsf{FE}}, \boldsymbol{K}_{n,0}^{(\alpha_j)}]$ is computed numerically. $\boldsymbol{K}_{n,0}^{(\alpha_j)}$ is computed analytically.

3.2.1. A torus with a circular crack and traction-free BCs.

The efficiency and accuracy of the QDFM is first checked by extracting the ESIFs for a simple problem of a torus with an inner crack. Consider a torus with an axis (which is a circle) of a radius $R = 1$, and a small radius of $1/2$, i.e. $\Omega = \{(\rho, \varphi, \theta) \,|\, 0 < \rho < 1/2, -\pi < \varphi < \pi, 0 \le \theta < 2\pi\}$. The radial coordinate r is bounded by $1/2 = r_1 < r < r_2 < 3/2$. A crack is inserted in the torus defined by $r < R = 1, x_3 = 0$ (see Figure 4, Left).

On the crack surfaces traction free boundary conditions are prescribed, whereas on the outer surface of the torus, $\rho = 1/2, 0 \le \theta < 2\pi$ the trace of the exact solution (22) up to $\mathcal{O}(\rho^4)$ is prescribed as Dirichlet BCs, with $A_{0_1} = A_{0_2} = A_{0_3} = A_4 =$

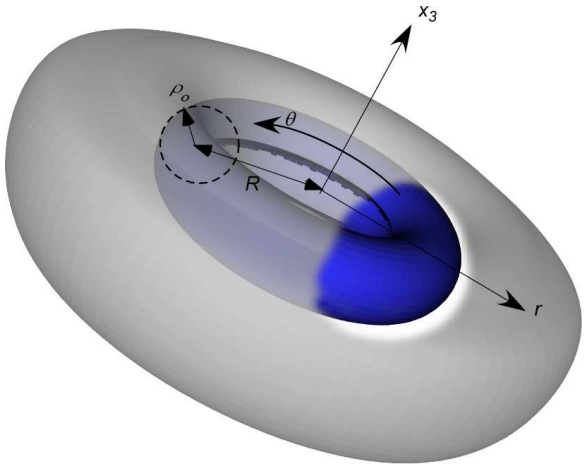

Figure 3: Domain with a circular singular edge and the integral surface.

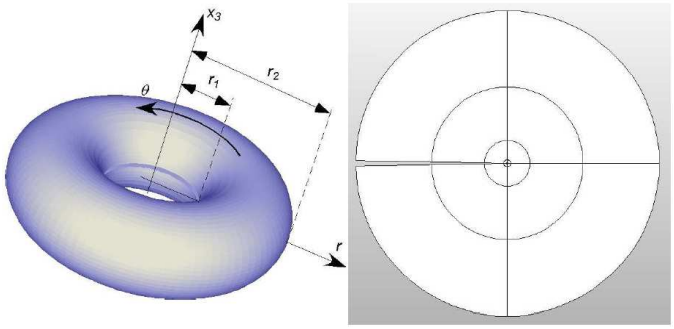

Figure 4: A torus with a circular crack and the axisymmetric finite element model.

$A_5 = A_6 = A_7 = \cdots = 0$, and $A_1 = A_2 = A_3 = 1$. The analytic formula for the boundary conditions coincides with the exact solution up to an order of $(\rho/R)^4$ due to the truncation of the series with respect to the index i .

Q_{ρ_0} is computed using a quadrature of order $90 (= n_{\mathsf{GP}})$ and $\boldsymbol{u}_{\mathsf{FE}}$ is extracted from a FE solution at $p = 8$ having an error of 0.32% in energy norm. The first three ESIFs A_1, A_2, A_3 are computed for different values of ρ_0 and different number of dual shadow functions n of QDF $\boldsymbol{K}_{n,0}^{(\alpha_j)}$. These relative errors for A_1, A_2, A_3 in % are summarized in Tables 1-3.

One notices the excellent results obtained as n increases or ρ_0/R tends to zero.

Table 1: % Relative error in A_1 for different numbers of shadow functions and different values of ρ_0/R for a circular crack with traction-free BCs.

	$\rho_0/R = 0.4$	$\rho_0/R = 0.3$	$\rho_0/R = 0.2$
$n = 0$	3.861	2.682	1.600
$n = 1$	4.763	2.868	1.276
$n = 2$	3.540	1.641	0.645
$n = 3$	1.238	0.310	0.085

Table 2: % Relative error in A_2 for different numbers of shadow functions and different values of ρ_0/R for a circular crack with traction-free BCs.

	$\rho_0/R = 0.4$	$\rho_0/R = 0.3$	$\rho_0/R = 0.2$
$n = 0$	30.970	17.545	8.338
$n = 1$	26.559	13.184	4.827
$n = 2$	11.806	3.600	0.102
$n = 3$	7.914	1.460	0.665

3.2.2. A penny shaped crack in an infinite domain under an axial uniform stress

Sneddon was the first to analyze a penny shaped crack of a radius R under an axial uniform stress σ_0 in an *infinite* domain [18]. For this case the stress intensity function is constant along the crack edge

$$K_I = 2\sigma_0\sqrt{\frac{R}{\pi}} \tag{42}$$

Remark 9. *In engineering terminology the stress intensity function is defined as:*

$$\lim_{\rho\to 0}\sigma_{\varphi\varphi}\frac{\rho^{1/2}\sqrt{2\pi}}{K_I} = 1 \tag{43}$$

Therefore, the connection between K_I and A_1 is obtained by inserting (43) *into* (B.1)*: $K_I = -4\mu\sqrt{2\pi}A_1$*

We construct a FE model of a cylinder with a radius b and height $H = 2b$ containing a penny-shaped crack of a radius $R = 1/2$ at its mid-height. An illustration of the problem is shown in Fig. 5 and the FE mesh in Fig. 6. The cylinder is loaded by an axial uniform stress $\sigma_0 = 1$ MPa, with the material properties $E = 20000$ MPa, $\nu = 0.3$

Table 3: % Relative error in A_3 for different numbers of shadow functions and different values of ρ_0/R for a circular crack with traction-free BCs.

	$\rho_0/R=0.4$	$\rho_0/R=0.3$	$\rho_0/R=0.2$
$n=0$	9.646	4.726	1.633
$n=1$	9.878	4.792	1.643
$n=2$	3.996	1.123	0.122
$n=3$	2.401	0.266	0.427

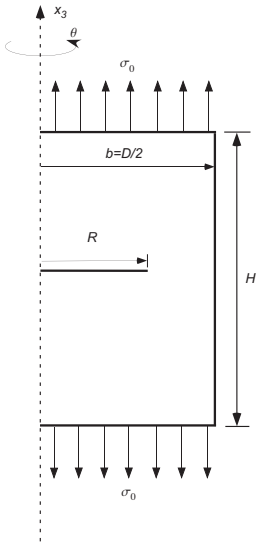

Figure 5: A cylinder with a penny-shaped crack under an axial uniform tension.

($\mu = 7692.31$ MPa , $\lambda = 11538.46$ MPa). *In all example problems in this section same material properties will be used and the integral* Q_{ρ_0} *is computed by using a quadrature of order* $90(= n_{\mathsf{GP}})$. $K_{I_{FE}}$ is extracted by $Q_{\rho_0=0.1}[\boldsymbol{u}_{FE}, \boldsymbol{K}_{4,0}^{(\alpha_1=1/2)}]$ for different radii b of the cylinder. The FE solution at $p=8$ has an error of 0.04% in energy norm. In Table 4 we compare the extracted $K_{I_{FE}}$ by $Q_{\rho_0=0.1}[\boldsymbol{u}, \boldsymbol{K}_{4,0}^{(1/2)}]$ to the exact SIF. For $b\to\infty, H\to\infty$, the SIF should tend to the value computed by Sneddon $K_{I_{Sneddon}} = 0.797885$.

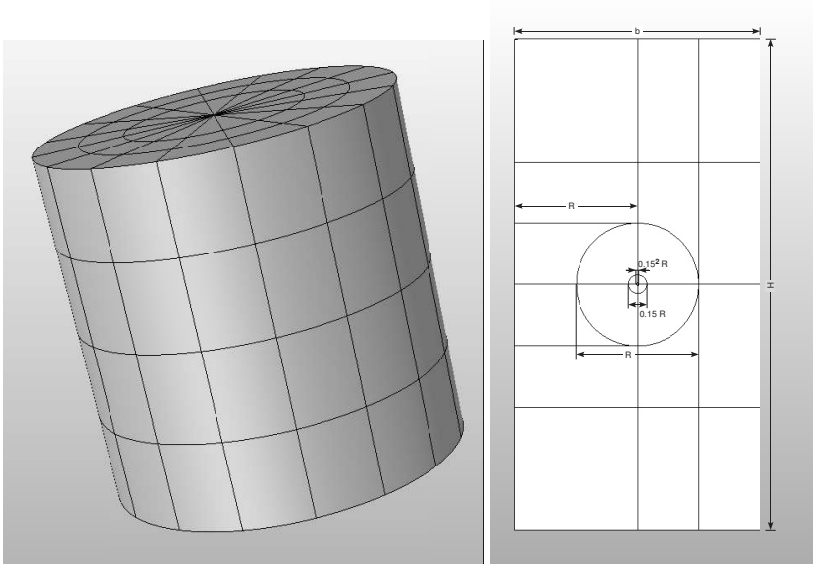

Figure 6: The FE model and mesh for a cylinder with a penny-shaped crack.

Table 4: The extracted $K_{I_{FE}}$ by $Q_{\rho_0=0.1}[\boldsymbol{u}_{FE}, \boldsymbol{K}^{(1/2)}_{4,0}]$

	$b=2.5$	$b=5$	$b=10$	$b=15$	$b=20$	$b=25$
$K_{I_{FE}}$	0.804678	0.798714	0.797928	0.797786	0.797574	0.797204
$\%\ relative\ error$	0.851319	0.103892	0.005331	0.012452	0.039020	0.085314

3.2.3. A finite cylinder with a penny-shaped crack under an axial uniform stress.

Benthem and Koiter analyzed a penny shaped crack in a finite long cylinder using an asymptotic method (see [2]). The stress intensity factor is given by:

$$K_I = \sigma_0\sqrt{\pi R}\left[\frac{b^2}{b^2-R^2}\sqrt{\frac{b-R}{b}}\left(\frac{2}{\pi}+\frac{R}{\pi b}-\frac{5R^2}{4\pi b^2}+0.268\frac{R^3}{b^3}\right)\right] \qquad (44)$$

For cylinder of finite radius no analytic results are available. Several FE and boundary element methods were used to extract the ESIFs for such a configuration, for example by [3, 12, 10, 6]. We solve the same problem for a cylinder of radius $b=1$ and height $H=2.8$ loaded by an axial uniform stress $\sigma_0=1$ containing a penny-shaped crack of a radius $R=1/2$ at the mid-height (FE mesh as in Figs. 6 is used).

$K_{I_{FE}}$ is computed by $Q_{\rho_0=0.1}[\boldsymbol{u}_{FE}, \boldsymbol{K}^{(\alpha_1=1/2)}_{n,0}]$ from a FE solution at $p=8$ having an error of 0.24% in energy norm. Because an exact ESIF is unavailable

we compute a "benchmark K_I" using the $Q_{\rho_0=0.001}[\boldsymbol{u}_{FE}, \boldsymbol{K}_{4,0}^{(\alpha_1=1/2)}]$, obtaining $K_I = 0.861594$. The relative error between the $K_{I_{FE}}$ and the benchmark value is reported in Table 5. The $K_{I_{FE}}$ computed by $Q_\rho[\boldsymbol{u}_{FE}, \boldsymbol{K}_{n,0}^{(1/2)}]$ is compared to

Table 5: $K_{I_{FE}}$ computed by $Q_{\rho_0=0.1}[\boldsymbol{u}_{FE}, \boldsymbol{K}_{n,0}^{(1/2)}]$ and the % of estimated relative error

	$n=0$	$n=1$	$n=2$	$n=3$	$n=4$
$K_{I_{FE}}$	0.857349	0.864749	0.859087	0.863598	0.861725
$\%\ estimated relative\ error\ in\ K_{I_{FE}}$	0.492647	0.366198	0.290935	0.232632	0.015219

[2, 3, 10, 12, 6], and to the value computed by a pointwise version of the contour integral method in StressCheck[1] in Table 6. The ESIF may be extracted accurately by

Table 6: K_I according to past publications

	Benthem &Koiter [2]	Chen et al. [3]	Kuo [10]	Leung&Su [12]	De Lacerda &Wrobel [6]	StressCheck at $\rho = 0.001$	$Q_{0.1}[\boldsymbol{u}_{FE}, \boldsymbol{K}_{4,0}^{(1/2)}]$
K_I	0.8624	0.8773	0.8557	0.8585	0.8598	0.8657	0.8617

the QDFM away from the singularities, without the need of a major mesh refinement.

3.2.4. Computing K_{III} : A finite cylinder with a penny shaped crack under torsion.

In the previous examples we only addressed K_I. Here we consider a penny-shaped crack in a finite long cylinder under torsion for which Benthem and Koiter have an approximate ESIF computed by asymptotic methods [2]):

$$K_{III} = \sigma_0\sqrt{\pi R}\frac{4b^3R}{3\pi\left(b^4-R^4\right)}\sqrt{\frac{b-R}{b}}\left(1+\frac{1}{2}\frac{R}{b}+\frac{3}{8}\frac{R^2}{b^2}+\frac{5}{16}\frac{R^3}{b^3}-\frac{93}{128}\frac{R^4}{b^4}+0.0038\frac{R^5}{b^5}\right) \tag{45}$$

For the same problem Kuo used the J_k integral combined with the finite element method [10] obtaining

$$K_{III} = 0.3763\sqrt{\sigma_0 R} \tag{46}$$

Consider a cylinder of radius $b = 1$ and height $H = 2.8$ containing a penny-shaped crack at the mid-height. The cylinder is loaded by torsion $T = (\sigma_0\pi b^3)/2 = \pi/2,\ (\sigma_0 = 1)$. The problem of interest and the BCs are shown in Fig.7 and the FE mesh is shown in Fig. 6.

[1] StressCheck is a trademark of ESRD, St. Louis, USA

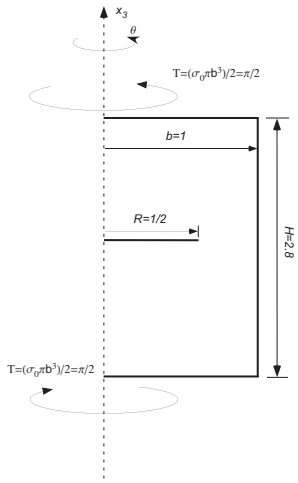

Figure 7: A cylinder with a penny-shaped crack under torsion.

$K_{III_{FE}}$ is computed by $Q_{\rho_0}[\boldsymbol{u}_{FE}, \boldsymbol{K}_{n,0}^{(\alpha_3=1/2)}]$ ($K_{III_{FE}} = \mu\sqrt{\pi/2}A_{3_{FE}}$) using a FE solution at $p = 8$ having an error of 0.11% in energy norm. The "benchmark $K_{III_{FE}}$ " is computed by $Q_{\rho_0=0.001}[\boldsymbol{u}_{FE}, \boldsymbol{K}_{4,0}^{(\alpha_3=1/2)}]$ obtaining $K_{III} = 0.268159$.

Table 7: Extracted $K_{III_{FE}}$ by $Q_{\rho_0=0.1}[\boldsymbol{u}, \boldsymbol{K}_{n,0}^{(1/2)}]$ and the % estimated relative error

	$n=0$	$n=1$	$n=2$	$n=3$	$n=4$	Benthem &Koiter [2]	Kuo [10]
$K_{III_{FE}}$	0.278360	0.274324	0.269480	0.268880	0.268540	0.268488	0.268276
$\%\ estimated\ rel.\ error$	3.714362	2.210723	0.405942	0.182345	0.055586		

3.2.5. A cylinder with a cylindrical crack

Here we address a cylindrical crack in a cylinder of radius $b = 10$ and height $H = 20$ under radial uniform pressure $P = 1$ that invokes mixed mode I and II ESIFs. The geometry and FE mesh are presented in Figures 9 and 8. The circular crack inclination in this case $-\pi/2 < \phi < 3\pi/2$ requires dual and shadow functions that are different compared to the penny shaped crack. These are provided in [16].

$K_{I_{FE}}$ and $K_{II_{FE}}$ are computed by by $Q_{\rho_0}[\boldsymbol{u}_{FE}, \boldsymbol{K}_{4,0}^{(\alpha_{1,2}=1/2)}]$ using $K_{I_{FE}} = -4\mu\sqrt{2\pi}A_{1_{FE}}$ and $K_{II_{FE}} = \frac{4}{3}\mu\sqrt{2\pi}A_{2_{FE}}$ and the FE solution at $p = 8$ having an error of 0.15% in energy norm. In Table 8, we compare $K_{I_{FE}}, K_{II_{FE}}$ to [7] and [3] and to the values computed by StressCheck.

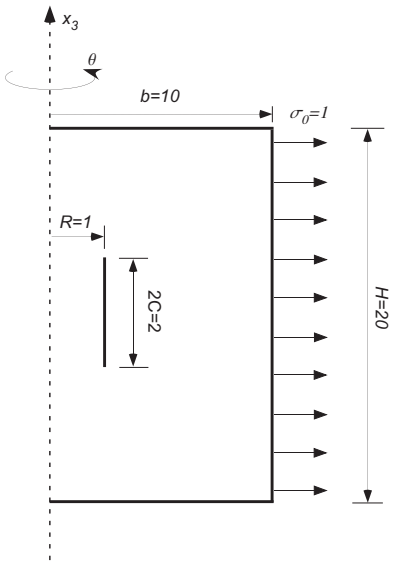

Figure 8: A cylinder with a cylindrical crack under radial uniform pressure.

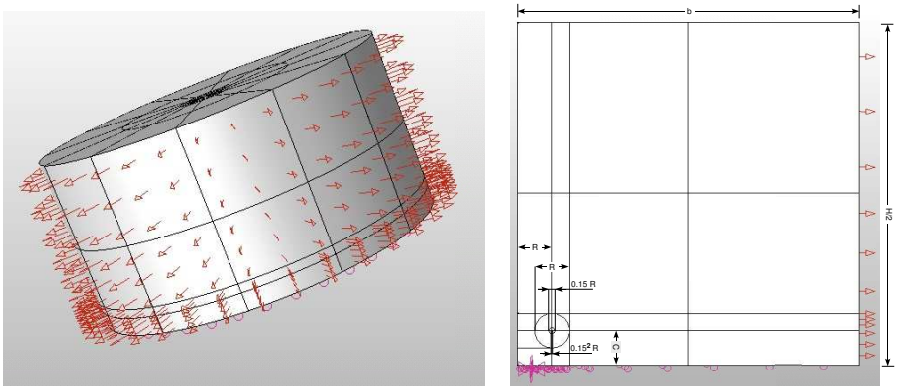

Figure 9: The FE mesh for a cylinder with a cylindrical crack.

3.2.6. A cylinder with an external circular crack

The determination of the angle interval in this case is $0 < \varphi < 2\pi$ and the crack faces are $\varphi_1 = 0$, $\varphi_2 = 2\pi$. Therefore, the primal, dual and shadow functions are different compared to the cracks considered herein and are provided in [16].

Consider a cylinder of a radius $b = 1$ and hight $H = 2.8$ with an external circular crack. The domain geometry and the mesh for this example problem are shown in Fig. 10. The cylinder is loaded by an axial uniform stress $\sigma_0 = 1$ and we extract $K_{I_{FE}}$ by the QDFM using a FE solution at $p = 8$ having an error of 0.71% in energy

Table 8: Extracted $K_{I_{FE}}$ & $K_{II_{FE}}$ by $Q_{\rho_0}[\boldsymbol{u}, \boldsymbol{K}_{4,0}^{(1/2)}]$ and the references values.

	$\rho_0/R =$					Demir et al.	Chen & Farris	StressCheck
	$1/2$	$1/4$	$1/10$	$1/20$	$1/40$	[7]	[3]	at $\rho = 0.0125$
K_I	0.8723	0.9568	0.9609	0.9606	0.9605	0.95	0.95	0.9391
K_{II}	0.1397	0.1484	0.1489	0.1489	0.1489	0.15	0.15	0.1486

norm. We summarize in Table 9 $K_{I_{FE}}$ extracted by $Q_{\rho_0=0.1}[\boldsymbol{u}, \boldsymbol{K}_{n,0}^{(1/2)}]$ for different

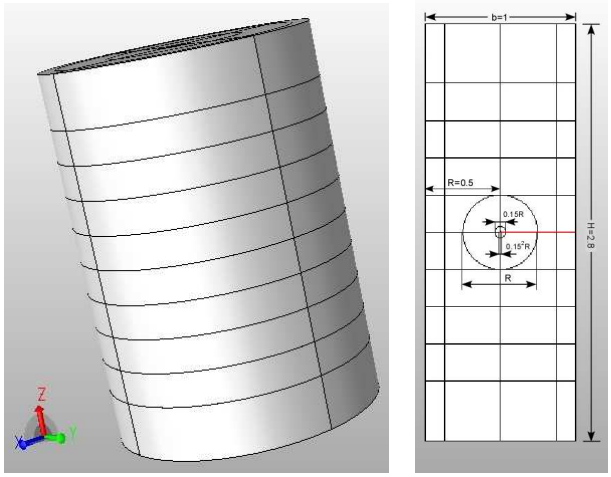

Figure 10: Domain and FE mesh for a cylinder with an external circular crack.

values of n. The estimated relative error is computed using the benchmark estimate $K_{I_{FE}} = 2.438603$ extracted by $Q_{\rho_0=0.001}[\boldsymbol{u}, \boldsymbol{K}_{4,0}^{(1/2)}]$.

Note that $K_{I_{FE}}$ in Table 9 is computed at a radius of $\rho_0 = 0.1$. The value extracted by $n = 4$ is compared to reference values presented in [2, 13, 9, 1, 12] and to the values computed by a pointwise algorithm at $\rho = 0.001$ in an axisymmetric FE model with a 0.3% error in energy norm in Table 10.

3.2.7. Influence of rigid body motion

We have noticed that the eigenfunctions associated with the integer eigenvalues are no longer orthogonal to the dual eigenfunctions associated with the halves eigenvalues (see Appendix C). This is especially important due to the rigid body displacements and rotations (associated with $\alpha_0, \alpha_1, \alpha_2 = 0$ and some of $\alpha_6, \alpha_7, \alpha_8 = 1$ eigenvalues that the crack edge almost always experiences). To demonstrate the influence of a rigid body motion on the ESIFs extracted by the QDFM we consider two cases that differ

Table 9: The extracted $K_{I_{FE}}$ by $Q_{\rho_0=0.1}[\boldsymbol{u}, \boldsymbol{K}_{n,0}^{(1/2)}]$ and the $\%$ estimated relative error.

	$n=0$	$n=1$	$n=2$	$n=3$	$n=4$
$K_{I_{FE}}$	2.4755	2.4263	2.4367	2.4394	2.4387
$\%\, estimated\, rel.\, error$	1.51388	0.50436	0.07809	0.03292	0.00263

Table 10: $K_{I_{FE}}$ extracted by $Q_{\rho_0=0.1}[\boldsymbol{u}, \boldsymbol{K}_{4,0}^{(1/2)}]$ compared to reference values.

	Benthem & Koiter [2]	Oglesby & Lomacky [13]	Hellen [9]	Bakr [1]	Leung & Su [12]	StressCheck at $\rho_0 = 0.001$	$Q_{0.1}[\boldsymbol{u}, \boldsymbol{K}_{4,0}^{(1/2)}]$
K_I	2.382	2.352	2.433	2.423	2.383	2.439	2.439

only by a single rigid body motion, see Fig. 11. On the cylinder in the left of Fig. 11 the BCs are such that the penny-shaped crack does not undergo a rigid body motion, whereas the right cylinder is identical to the left one, but includes a rigid body motion in the z direction. The FE meshes for this example problem are as in Fig. 6.

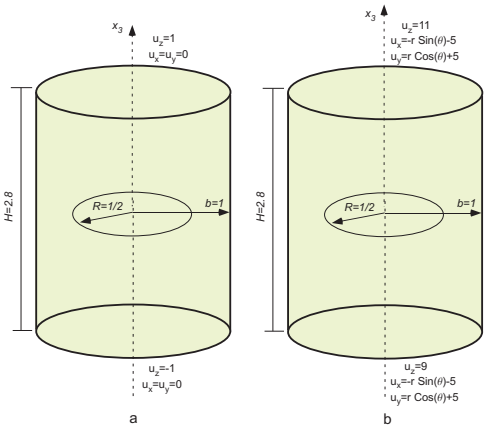

Figure 11: A cylinder with a penny shaped crack and the BCs: (a) Without a rigid body motion, (b) with a rigid body motion.

$K_{I_{FE}}, K_{II_{FE}}$ and $K_{III_{FE}}$ extracted by $Q_{\rho_0}[\boldsymbol{u}_{FE}, \boldsymbol{K}_{n,0}^{(\alpha_{1,2,3}=1/2)}]$ for the two cases compared to the benchmark values computed by $Q_{0.001}[\boldsymbol{u}_{FE}, \boldsymbol{K}_{4,0}^{(\alpha_{1,2,3})}]$ are summarized in Table 11.

The example demonstrates that the rigid body motion in z direction and rotation along the $x-y$ plane has only an influence on the computation of K_{II} but as the

Table 11: $K_{I_{FE}}$, $K_{II_{FE}}$ & $K_{III_{FE}}$ and the reference values

without a rigid body motion						
	$n=0$	$n=1$	$n=2$	$n=3$	$n=4$	benchmark value
$K_{I_{FE}}$	12002.38	12106.93	12024.88	12089.18	12062.61	12060.83
$K_{II_{FE}}$	0.32	0.37	0.54	0.56	0.57	1.27
$K_{III_{FE}}$	-0.01	-0.01	-0.01	-0.01	-0.01	1.54
with a rigid body motion						
	$n=0$	$n=1$	$n=2$	$n=3$	$n=4$	benchmark values
$K_{I_{FE}}$	12002.38	12106.93	12024.88	12089.18	12062.61	12060.83
$K_{II_{FE}}$	-40665.55	5262.29	-4374.66	148.17	-150.25	1.27
$K_{III_{FE}}$	-0.01	-0.01	-0.01	-0.01	-0.01	1.54

order of the QDF increases, the influence decreases. For $n = 4$ one notices that the value of K_{II} (although not zero) is 2 orders of magnitude smaller compared to K_I .

4. Non-axisymmetric case

For a general non-axisymmetric case, the solution $\boldsymbol{u}$ is given by (1), and the QDF depends on θ through the extraction functions $B_j(\theta)$:

$$\boldsymbol{K}_{n,m}^{(\alpha_j)}(\rho,\varphi,\theta) \stackrel{\text{def}}{=} \sum_{h=0,2,4\cdots}^{m} \partial_\theta^h B_j(\theta)\rho^{-\alpha_j} \sum_{f=0}^{n} \left(\frac{\rho}{R}\right)^{h+f} \boldsymbol{\psi}_{hjf}(\varphi) \tag{47}$$

For a circular *closed* edge $(\theta \in [0, 2\pi])$ the ESIF $A_k(\theta)$ and their derivatives are continuous along the edge so they may be expanded as a Fourier series

$$\tilde{A}_{k_P}(\theta) = a_{k_0} + \sum_{p=1}^{P} a_{k_{2p-1}} \cos(p\theta) + \sum_{p=1}^{P} a_{k_{2p}} \sin(p\theta). \tag{48}$$

In analogy to [21], for extracting each of the coefficients a_{j_q}, we need to choose a specific $B_{j_q}(\theta)$ such that:

$$Q_{\rho_0}[\boldsymbol{u}, \boldsymbol{K}_{n,m}^{(\alpha_j)}(B_{j_q})] = a_{j_q} + \mathcal{O}\left(\frac{\rho_0}{R}\right)^{s(n,m)}. \tag{49}$$

Therefore it is desired that an orthogonality relation be imposed between $B_{j_q}(\theta)$ and $\sin(p\theta)$ or $\cos(p\theta)$. These are chosen as

$$B_{j_{2q-1}}(\theta) = b_{j_{2q-1}} \cos(q\theta) \quad \text{or} \quad B_{j_{2q}}(\theta) = b_{j_{2q}} \sin(q\theta). \tag{50}$$

To obtain precisely a_{j_q} alone, one must choose b_{j_q} such that $\lim_{\rho_0/R\to 0}\left\{Q_{\rho_0}\left[\boldsymbol{u}, \boldsymbol{K}_{0,0}^{(\alpha_j)}(B_{j_q})\right]\right\} = a_{j_q}$. This b_{j_q} is be obtained by evaluating $\lim_{\rho_0/R\to 0}\left\{Q_{\rho_0}\left[\boldsymbol{u}, \boldsymbol{K}_{n,m}^{(\alpha_j)}\right]\right\} = \lim_{\rho_0/R\to 0}\left\{Q_{\rho_0}\left[\boldsymbol{u}, \boldsymbol{K}_{0,0}^{(\alpha_j)}\right]\right\}$.

Inserting (1) and (47) with $A_k(\theta)$ represented by (48) and $B_{j_q}(\theta)$ in (50) to (7), one obtains the following expressions for b_{j_q} . For ESIFs associated with mode I and mode II (i.e. $A_1, A_2, A_7, A_8, A_{13}, A_{14}\cdots$), b_{j_q} is:

$$b_{j_0} = \frac{\left(\alpha_j^2 - 1\right)(\lambda+\mu)}{32\pi^2\alpha_j\mu(\lambda+2\mu)R}, \quad q = 0 \tag{51}$$

$$b_{j_q} = \frac{\left(\alpha_j^2 - 1\right)(\lambda+\mu)}{16\pi^2\alpha_j\mu(\lambda+2\mu)R}, \quad q \neq 0 \tag{52}$$

For ESIFs associated with mode III (i.e. $A_3, A_9, A_{15}\cdots$), b_{j_q} is:

$$b_{j_0} = \frac{1}{4\pi^2\alpha_j\mu R}, \quad q = 0 \tag{53}$$

$$b_{j_q} = \frac{1}{2\pi^2\alpha_j\mu R}, \quad q \neq 0 \tag{54}$$

For a penny-shaped crack, for example, with homogenous Neumann BCs, $\omega = 2\pi$, $(\varphi_1 = -\pi, \varphi_2 = \pi)$ we compute $Q_{\rho_0}[\boldsymbol{u}, \boldsymbol{K}_{n,m}^{(\alpha_j)}(B_{j_q})]$ analytically for different n and m. We represent $\boldsymbol{u}$ up to order of $\rho^{9/2}$ (the explicit expressions for $\phi_{\ell,k,i}$ and $\psi_{\ell,k,i}$ are provided in [16]). The Fourier coefficients a_{j_q} are obtained by (13) as follows:

$$Q_{\rho_0}[\boldsymbol{u}, \boldsymbol{K}_{n,m}^{(\alpha_j)}(B_{j_q})] = a_{j_q} + \mathcal{O}\left\{\rho_0^{\alpha_0-\alpha_1}\left[\left(\frac{\rho_0}{R}\right)^{n+1} + \left(\frac{\rho_0}{R}\right)^{m+1}\right]\right\} \tag{55}$$

4.1. Numerical examples

4.1.1. A cylinder with a penny-shaped crack in bending

Benthem and Koiter analyzed a penny shaped crack in a long cylinder under bending using an asymptotic method [2]. They report the maximum stress intensity factor

$$K_I = \frac{4\sigma_0}{3\sqrt{\pi}}\frac{b^2 R}{b^4 - R^4}\sqrt{\frac{(b-R)R}{b}}\left(1 + \frac{1}{2}\frac{R}{b} + \frac{3}{8}\left(\frac{R}{b}\right)^2 + \frac{5}{16}\left(\frac{R}{b}\right)^3 - \frac{93}{128}\left(\frac{R}{b}\right)^4 + 0.483\left(\frac{R}{b}\right)^5\right) \tag{56}$$

Kuo used the J_k integral in combination with the finite element method to extract the stress intensity function for a penny-shaped crack in a finite cylinder under bending (see [10]):

$$K_I(\theta) = \left(0.3762\sqrt{\sigma_0 R}\right)\sin\theta \tag{57}$$

We consider a cylinder with a radius $b = 1$ and height $H = 2.8$ containing a penny-shaped crack of radius $R = 1/2$ at the mid-height loaded by a bending moment $M = \sigma_0 \pi b^2/4 = \pi/4$ as shown in Fig. 12. The FE mesh is the same one presented in Fig 6.

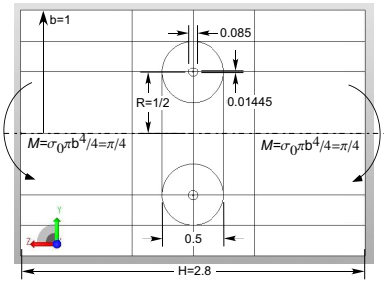

Figure 12: A cylinder with a penny-shaped crack under bending BCs.

We extract $\tilde{K}_{I_{FE}}(\theta)$ by $Q_{\rho_0}[\boldsymbol{u}_{FE}, \boldsymbol{K}_{n,m}^{(\alpha_1=1/2)}(B_{j_q})]$ with $K_{I_{FE}}(\theta) = -4\mu\sqrt{2\pi}A_{1_{FE}}(\theta)$ and the FE solution at $p = 8$ having an error of 0.15% in energy norm.

The amplitude of $K_{I_{FE}}(\theta)$ computed by $Q_{\rho_0=0.1}[\boldsymbol{u}_{FE}, \boldsymbol{K}_{n,m}^{(\alpha_1=1/2)}(B_{1_q})]$ is compared to the reference values in [2, 10] in Table 12.

We also obtain that $a_{1p} \approx 0$ for all $p \neq 2$, demonstrating the the ESIF functional representation is $\sin(\theta)$ as expected. The ESIF $\tilde{K}_I(\theta)$ for the different n s are shown

Table 12: Maximum value of K_I (the $\sin\theta$ coefficient) computed by $Q_{0.1}[\boldsymbol{u}_{FE}, \boldsymbol{K}^{(1/2)}_{n,n}(B_{1_2})]$

$n=0$	$n=1$	$n=2$	$n=3$	Benthem&Koiter [2]	Kuo [10]
0.296589	0.274168	0.266477	0.271342	0.271317	0.266013

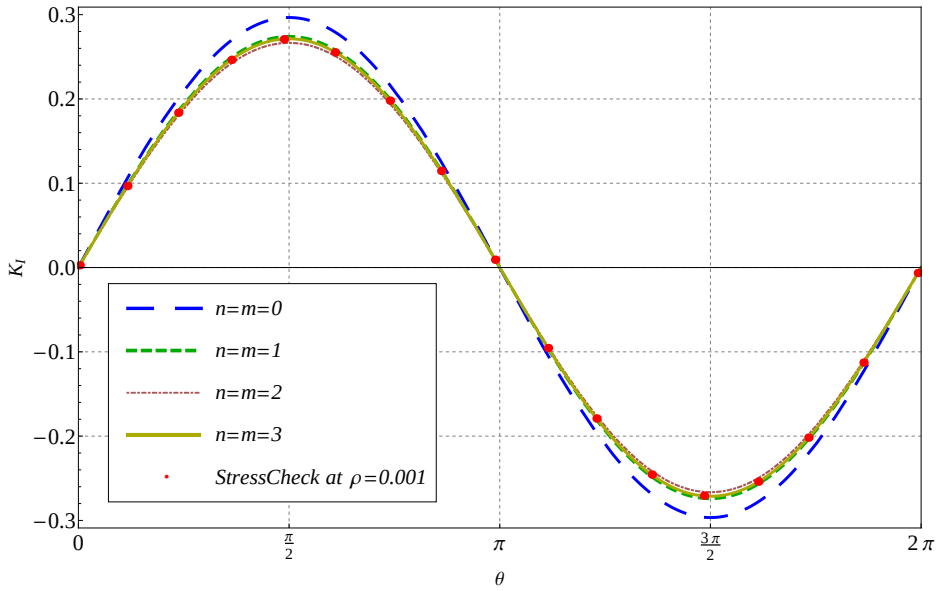

Figure 13: Extracted $\tilde{K}_I(\theta)$ by $Q_{\rho_0=0.1}[\boldsymbol{u}, \boldsymbol{K}^{(1/2)}_{n,m=n}[B_{1_q}]]$ at $\rho_0 = 0.1$ and the pointwise values at $\rho_0 = 0.001$.

in Fig. 13 compared to the point-wise values computed at $\rho_0 = 0.001$. This example demonstrates that a very accurate functional representation of the ESIF can be obtained as n increases using an extraction radius which is 20% of the crack radius - therefore, the FE mesh does not need to be refined considerably towards the singular edge.

4.1.2. An inclined penny-shaped crack in a cube under a general load

The last example is an inclined penny-shaped crack in a cube, that excites all ESIFs. Consider a $\sqrt{12.5} \times \sqrt{12.5} \times \sqrt{12.5}$ cube with a penny-shaped crack of radius $R = 1/2$ at its center inclined at an angle of 45^o with respect to the y axis (the normal to the crack plane is along z direction), see Fig. 14. The left upper face of the cube is loaded by a unit traction in the x and y directions and three other faces are subject to symmetric BCs.

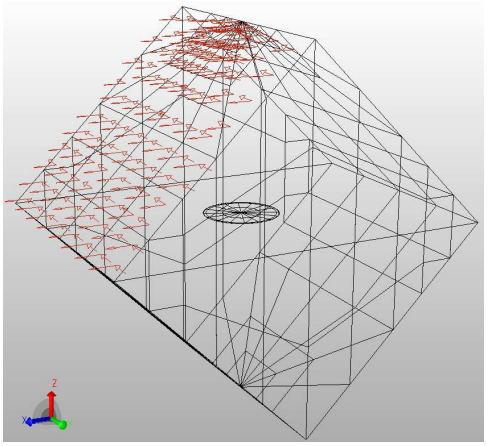

Figure 14: FE model of the cube with an inclined penny-shaped crack including the loading BCs.

We extract $\tilde{K}_{I_{FE}}(\theta), \tilde{K}_{II_{FE}}(\theta), \tilde{K}_{III_{FE}}(\theta)$ by $Q_{\rho_0}[\boldsymbol{u}_{FE}, \boldsymbol{K}_{n,n}^{(\alpha_{1,2,3}=1/2)}(B_{j_q})]$. The integral $Q_{0.1}$ is computed by using a quadrature of order $90(= n_{\mathsf{GP}})$ and $\boldsymbol{u}_{\mathsf{FE}}$ is extracted from a FE solution at $p = 8$ having an error of 1.34% in energy norm. The FE model contains 720 elements and 181000 degrees of freedom with three layers around the circular crack of dimensions $0.25, 0.25 * 0.15, 0.25 * 0.15^2$. We used nine extraction functions B_{j_q} to compute the nine $a_{j_1}, \cdots, a_{j_9}$ (their values are provided in Appendix D). To estimate the relative error, the extracted ESIFs at $\rho = 0.001$ and $n = 3$ were used as benchmarks. We also used the pointwise extraction method available in the FE code StressCheck to compute at specific points along the edge K_I and K_{II} (the algorithm in StressCheck cannot compute K_{III}) at $\rho = 0.001$ to double verify the benchmark data. In Figures 15-17 we present the functional representation of the first three stress intensity functions along the crack front (computed using the extracted a_{j_q}) and the estimated relative error in percentage as n increases. The convergence of the extracted ESIFs to the benchmark functions is clearly visible as n increases, although the extraction radius is relatively large.

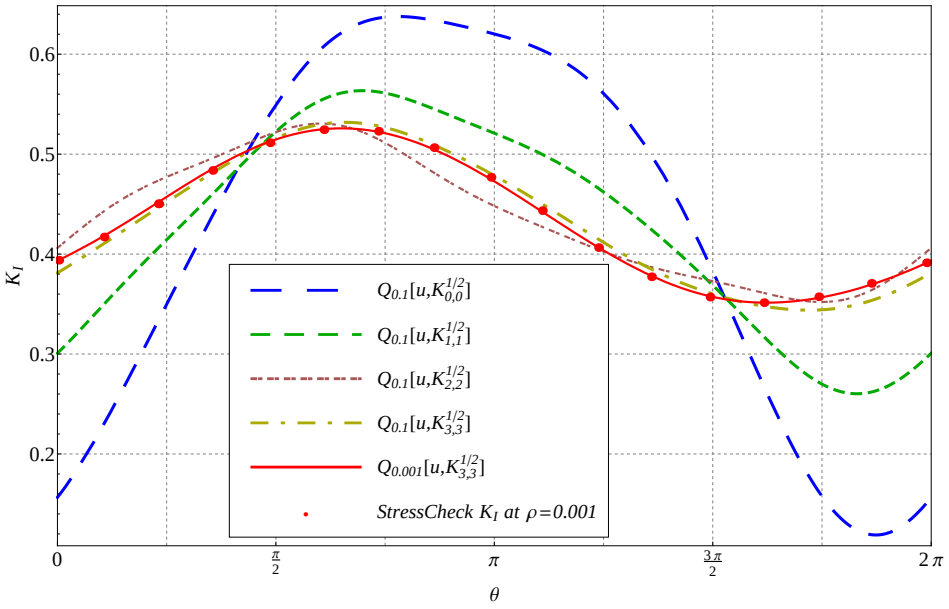

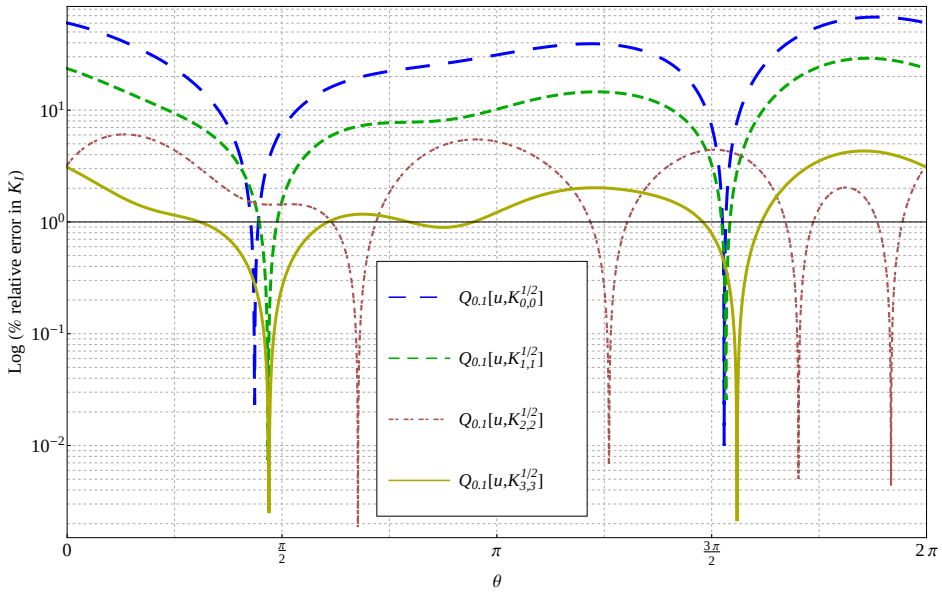

Figure 15: The extracted K_I and the % relative error in K_I .

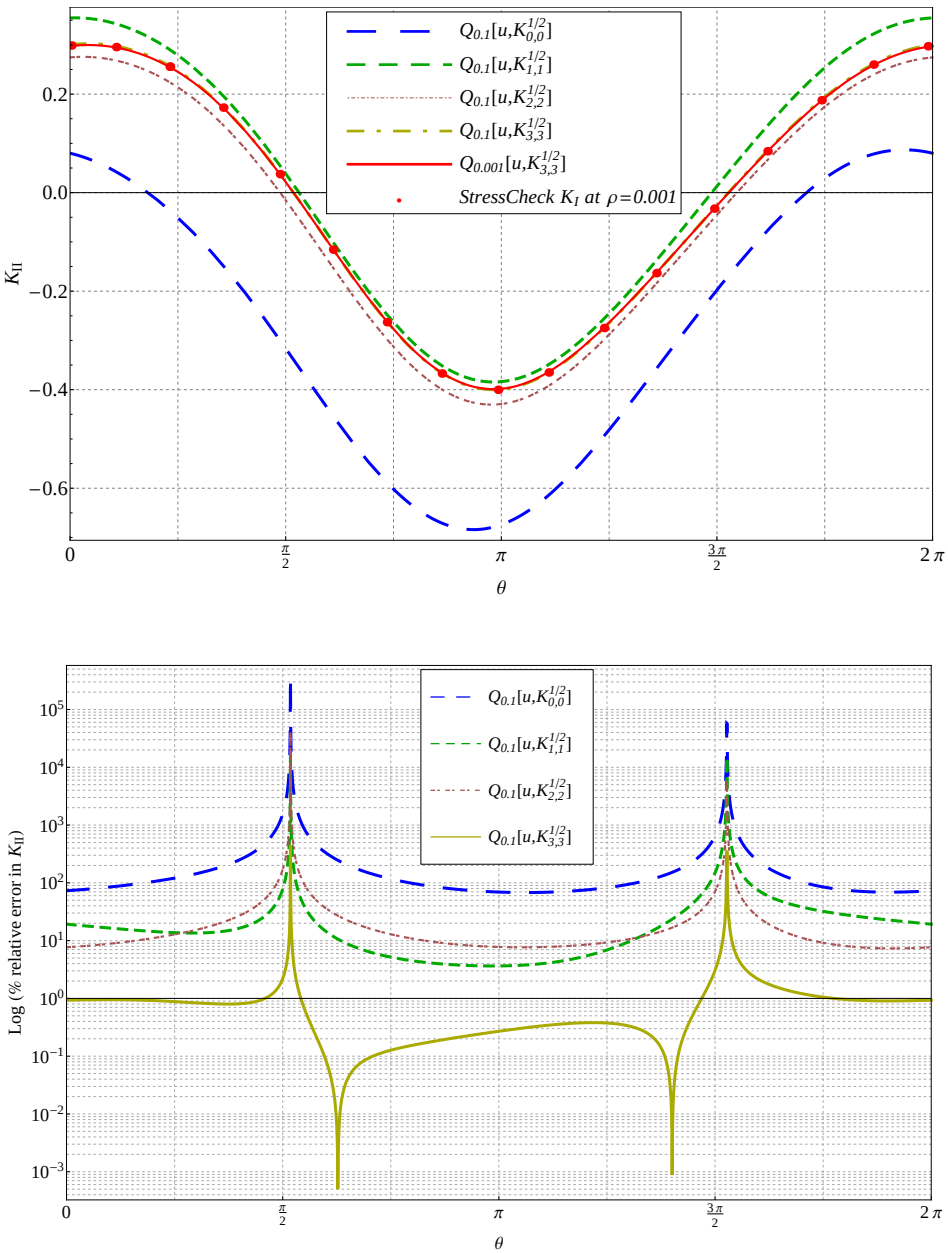

Figure 16: The extracted K_{II} and the % relative error in K_{II} .

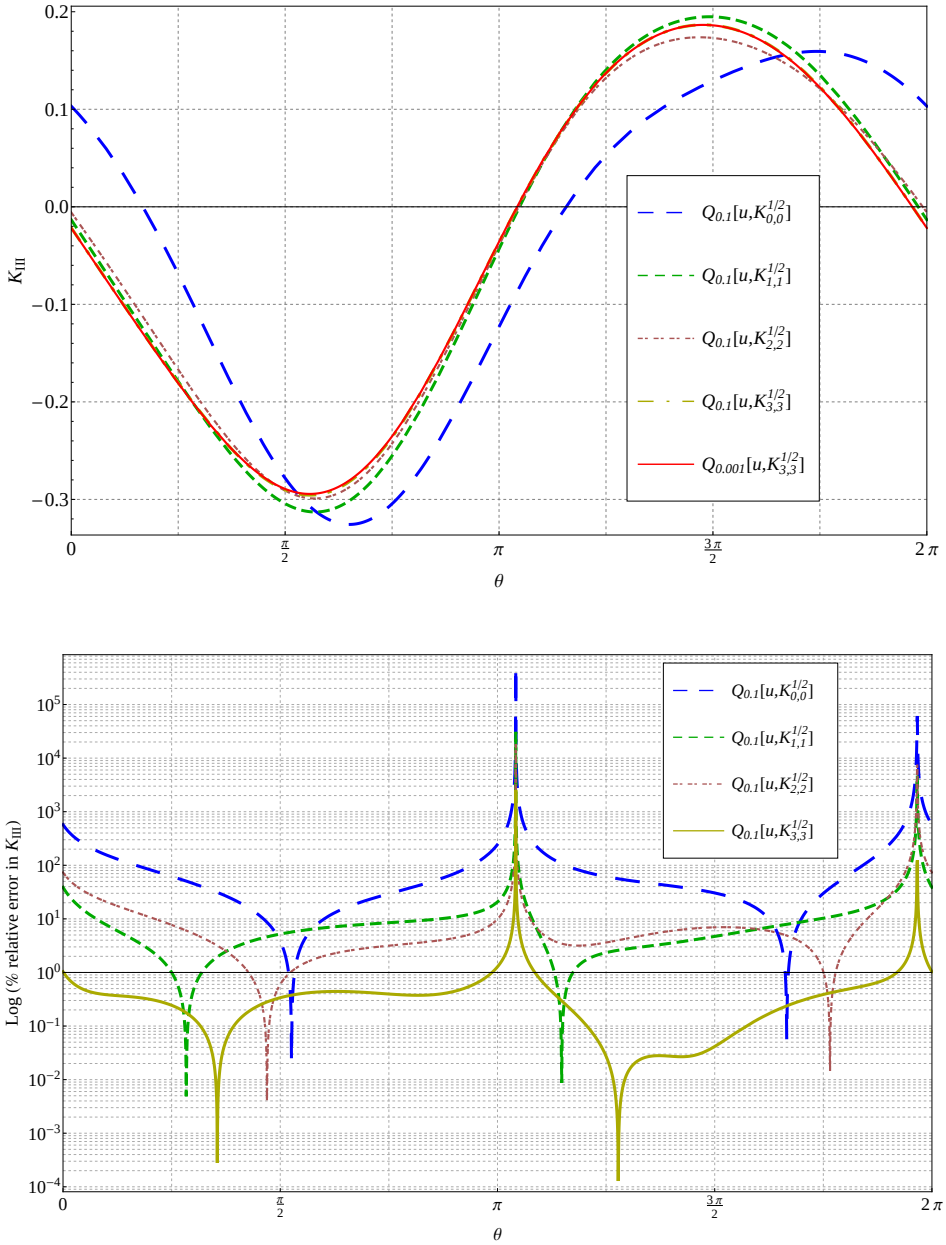

Figure 17: The extracted K_{III} and the % relative error in K_{III} .

5. Summary and Conclusions

The QDFM introduced in [17] for circular singular edges in the framework of the Laplace equation has been extended to the elasticity system. We demonstrated that one may compute the edge stress intensity functions with high accuracy from p-FE models for axisymmetric as well as non axisymmetric cases. One of the most important advantages of the present method is that the required data from a FE model can be retrieved away from the singular edge therefore one does not need to considerably refine the mesh in the vicinity of the crack front. Any ESIF can be extracted having a functional representation (and not only pointwise values along the edge). Although we considered in this paper only circular cracks, the method is equally applicable to any singular circular edge (V-notches for example), and we restricted our attention to cracks due to their special engineering importance.

For the extraction of ESIFs of higher indexes $A_j, A_{j+1}...$, with $j \leq 7$, associated with eigenvalues for which $\alpha_j = \alpha_i + q, \quad q \in \mathbb{N}$, the case of resonance illustrated in [17] may occur. For these situations one needs to modify the QDF so to include another shadow function $\boldsymbol{\psi}_{0,j,1}$. This case is not addressed here due to being only a technical procedure.

Several numerical example problems have been presented which demonstrate the robustness, accuracy and efficiency of the QDFM when applied in conjunction with the p-version of the FE method.

One of the topics which is still under investigation is the computation of dual eigenfunctions associated with the integer eigenvalues $(\alpha_j \in \mathbb{N})$. The algorithm in Appendix A is inappropriate for the integer eigenvalues and further research is necessary for their determination. Also, the new QDFM may be used for extracting ESIFs for more realistic and intrigue problems of planar cracks of various shapes (elliptical cracks for example, and cracks that terminate at the free surface). These topics are under research and will be reported in future publications.

Acknowledgements

The authors thank Profs. Monique Dauge and Martin Costabel, IRMAR, University of Rennes 1, France for helpful discussions and insights. This research was supported by the Israel Science Foundation (grant No. 444/10).

Appendix A. The dual-eigenfunctions $\boldsymbol{\psi_{h,j,f}}$

Eigenfunctions and their shadows are obtained by a recursive set of equations given in [22]. The dual eigenfunctions and their shadows $\boldsymbol{\psi}_{h,j,f}(\varphi) = \left(\psi^{\rho}_{h,j,f}, \psi^{\varphi}_{h,j,f}, \psi^{\theta}_{h,j,f}\right)^T$ are obtained by the same recursive set of equations as for the primal eigenfunctions and shadows with $-\alpha_j$ instead of α_j :

$$
\begin{aligned}
[m_0]\boldsymbol{\psi}_{h,j,f} \quad = \quad & -\left(2\cos\varphi[m_0] + [m_{01}]\right)\boldsymbol{\psi}_{h,j,f-1} - \left(\cos^2\varphi[m_0] + \cos\varphi[m_{01}] + [m_{02}]\right)\boldsymbol{\psi}_{h,j,f-2} \\
& -[m_{10}]\boldsymbol{\psi}_{h-1,j,f} - \left(\cos\varphi[m_{10}] + [m_{11}]\right)\boldsymbol{\psi}_{h-1,j,f-1} - [m_2]\boldsymbol{\psi}_{h-2,j,f}, \qquad h \geq 0,\ f \geq 0
\end{aligned}
$$

$\boldsymbol{\psi}$ s having negative indices are set to zero. The $[m]$ s are differential operators given by (we denote $\beta = -\alpha_j + h + f$):

$$[m_0]\boldsymbol{\psi}_{h,j,f} = \begin{pmatrix} (\lambda+2\mu)\left(\beta^2-1\right)+\mu\partial_{\varphi\varphi} & ((\lambda+\mu)\beta-(\lambda+3\mu))\,\partial_\varphi & 0 \\ ((\lambda+\mu)\beta+(\lambda+3\mu))\,\partial_\varphi & \mu\left(\beta^2-1\right)+(\lambda+2\mu)\partial_{\varphi\varphi} & 0 \\ 0 & 0 & \mu\left(\beta^2+\partial_{\varphi\varphi}\right) \end{pmatrix} \boldsymbol{\psi}_{h,j,f}$$

$$[m_{01}]\boldsymbol{\psi}_{h,j,f} = \begin{pmatrix} (\lambda+2\mu)\cos\varphi\beta-\mu\sin\varphi\partial_\varphi & \sin\varphi\,(\mu-(\lambda+\mu)\beta) & 0 \\ -(\lambda+2\mu)\sin\varphi+(\lambda+\mu)\cos\varphi\partial_\varphi & \cos\varphi\,(\mu\,(\beta-1)-\lambda)-(\lambda+2\mu)\sin\varphi\partial_\varphi & 0 \\ 0 & 0 & \mu\,(\beta\cos\varphi-\sin\varphi\partial_\varphi) \end{pmatrix} \boldsymbol{\psi}_{h,j,f}$$

$$[m_{02}]\boldsymbol{\psi}_{h,j,f} = \begin{pmatrix} -(\lambda+2\mu)\cos^2\varphi & (\lambda+2\mu)\cos\varphi\sin\varphi & 0 \\ (\lambda+2\mu)\sin\varphi\cos\varphi & -(\lambda+2\mu)\sin^2\varphi & 0 \\ 0 & 0 & -\mu \end{pmatrix} \boldsymbol{\psi}_{h,j,f}$$

$$[m_{10}]\boldsymbol{\psi}_{h,j,f} = \begin{pmatrix} 0 & 0 & (\lambda+\mu)\beta \\ 0 & 0 & (\lambda+\mu)\partial_\varphi \\ (\lambda+\mu)(\beta+1) & (\lambda+\mu)\partial_\varphi & 0 \end{pmatrix} \boldsymbol{\psi}_{h,j,f}$$

$$[m_{11}]\boldsymbol{\psi}_{h,j,f} = \begin{pmatrix} 0 & 0 & -(\lambda+3\mu)\cos\varphi \\ 0 & 0 & (\lambda+3\mu)\sin\varphi \\ (\lambda+3\mu)\cos\varphi & -(\lambda+3\mu)\sin\varphi & 0 \end{pmatrix} \boldsymbol{\psi}_{h,j,f}$$

$$[m_2]\boldsymbol{\psi}_{h,j,f} = \begin{pmatrix} \mu & 0 & 0 \\ 0 & \mu & 0 \\ 0 & 0 & (\lambda+2\mu) \end{pmatrix} \boldsymbol{\psi}_{h,j,f}$$

For clamped or traction-free BCs:

$$\psi^{\rho}_{h,j,f} = \psi^{\varphi}_{h,j,f} = \psi^{\theta}_{h,j,f} = 0 \qquad \text{on } \Gamma_1 \cup \Gamma_2 \qquad \text{Clamped BCs.}$$

$$[t_0]\,\boldsymbol{\psi}_{h,j,f} = -\left([t_1] + \cos\varphi\,[t_0]\right)\boldsymbol{\psi}_{h,j,f-1} - [t_2]\,\boldsymbol{\psi}_{h-1,j,f} \qquad \text{on } \Gamma_1 \cup \Gamma_2 \qquad \text{Traction-free BCs.}$$

$\boldsymbol{\psi}_{h,j,f}$ s with negative index are zero, and

$$[t_0]\,\boldsymbol{\psi}_{h,j,f} \quad = \quad \begin{pmatrix} \mu\partial_\varphi & \mu\,(\beta-1) & 0 \\ 2\mu+\lambda\,(\beta+1) & (\lambda+2\mu)\partial_\varphi & 0 \\ 0 & 0 & \mu\partial_\varphi \end{pmatrix} \boldsymbol{\psi}_{h,j,f}$$

$$[t_1]\,\boldsymbol{\psi}_{h,j,f} \quad = \quad \begin{pmatrix} 0 & 0 & 0 \\ \lambda\cos\varphi & -\lambda\sin\varphi & 0 \\ 0 & 0 & \mu\sin\varphi \end{pmatrix} \boldsymbol{\psi}_{h,j,f}$$

$$[t_2]\,\boldsymbol{\psi}_{h,j,f} \quad = \quad \begin{pmatrix} 0 & 0 & 0 \\ 0 & 0 & \lambda \\ 0 & \mu & 0 \end{pmatrix} \boldsymbol{\psi}_{h,j,f}$$

Appendix B. The stress-displacements connections in ρ, φ, z coordinates

Having the displacement vector in ρ, φ, z coordinates, then the corresponding stress vector (under the assumption of an isotropic material) is given by:

$$\begin{pmatrix} \sigma_{\rho\rho} \\ \sigma_{\theta\theta} \\ \sigma_{\varphi\varphi} \\ \sigma_{\rho\theta} \\ \sigma_{\rho\varphi} \\ \sigma_{\theta\varphi} \end{pmatrix} = \begin{pmatrix} \lambda\frac{1}{\rho} + (\lambda+2\mu)\partial_\rho & \lambda\frac{1}{\rho}\partial_\varphi & 0 \\ \lambda\left(\frac{1}{\rho} + \partial_\rho\right) & \lambda\frac{1}{\rho}\partial_\varphi & 0 \\ (\lambda+2\mu)\frac{1}{\rho} + \lambda\partial_\rho & (\lambda+2\mu)\frac{1}{\rho}\partial_\varphi & 0 \\ 0 & 0 & \mu\partial_\rho \\ \mu\frac{1}{\rho}\partial_\varphi & \mu\left(-\frac{1}{\rho} + \partial_\rho\right) & 0 \\ 0 & 0 & \mu\frac{1}{\rho}\partial_\varphi \end{pmatrix} \begin{pmatrix} u_\rho \\ u_\varphi \\ u_\theta \end{pmatrix} \tag{B.1}$$

$$+\frac{1}{R}\frac{1}{1+\frac{\rho}{R}\cos\varphi} \begin{pmatrix} \lambda\cos\varphi & -\lambda\sin\varphi & 0 \\ (\lambda+2\mu)\cos\varphi & -(\lambda+2\mu)\sin\varphi & 0 \\ \lambda\cos\varphi & -\lambda\sin\varphi & 0 \\ 0 & 0 & -\mu\cos\varphi \\ 0 & 0 & 0 \\ 0 & 0 & \mu\sin\varphi \end{pmatrix} \begin{pmatrix} u_\rho \\ u_\varphi \\ u_\theta \end{pmatrix}$$

$$+\frac{1}{R}\frac{1}{1+\frac{\rho}{R}\cos\varphi} \begin{pmatrix} 0 & 0 & \lambda \\ 0 & 0 & \lambda+2\mu \\ 0 & 0 & \lambda \\ \mu & 0 & 0 \\ 0 & 0 & 0 \\ 0 & \mu & 0 \end{pmatrix} \partial_\theta \begin{pmatrix} u_\rho \\ u_\varphi \\ u_\theta \end{pmatrix}$$

Appendix C. The non-orthogonality between the primal eigenfunctions $\boldsymbol{\phi_{0,0,0}}$ and the primal dual eigenfunctions $\boldsymbol{\psi_{0,1,0}}$

We demonstrate that no orthogonality exists between the primal eigenfunctions that correspond to the zero eigenvalue $\boldsymbol{\phi}_{0,0,0}$ and the primal dual eigenfunctions that correspond to $\alpha_j = 1/2:\ \boldsymbol{\psi}_{0,1,0}\,,\ \boldsymbol{\psi}_{0,2,0}\,,\ \boldsymbol{\psi}_{0,3,0}\,.$

For a penny-shaped crack with traction-free BCs, the first primal eigenfunctions $\boldsymbol{\phi}_{0,0_1,0}, \boldsymbol{\phi}_{0,0_2,0}, \boldsymbol{\phi}_{0,0_3,0}$ associated with the eigenvalues $\alpha_{0_1} = \alpha_{0_2} = \alpha_{0_3} = 0$ are

$$\boldsymbol{\phi}_{0,0_1,0} = \begin{pmatrix} \cos\varphi \\ -\sin\varphi \\ 0 \end{pmatrix}, \qquad \boldsymbol{\phi}_{0,0_2,0} = \begin{pmatrix} \sin\varphi \\ \cos\varphi \\ 0 \end{pmatrix}, \qquad \boldsymbol{\phi}_{0,0_3,0} = \begin{pmatrix} 0 \\ 0 \\ 1 \end{pmatrix}. \tag{C.1}$$

The first singular dual eigenfunctions which belong to the dual eigenvalues $\alpha_1 = \alpha_2 = \alpha_3 = -1/2$ are

$$\boldsymbol{\psi}_{0,1,0} = \begin{pmatrix} \cos\frac{\varphi}{2} - \frac{3\lambda+7\mu}{3(\lambda+\mu)}\cos\frac{3\varphi}{2} \\ -\sin\frac{\varphi}{2} + \frac{\lambda+5\mu}{3(\lambda+\mu)}\sin\frac{3\varphi}{2} \\ 0 \end{pmatrix}, \qquad \boldsymbol{\psi}_{0,2,0} = \begin{pmatrix} \sin\frac{\varphi}{2} - \frac{3\lambda+7\mu}{\lambda+\mu}\sin\frac{3\varphi}{2} \\ \cos\frac{\varphi}{2} - \frac{\lambda+5\mu}{\lambda+\mu}\cos\frac{3\varphi}{2} \\ 0 \end{pmatrix}, \tag{C.2}$$

$$\boldsymbol{\psi}_{0,3,0} = \begin{pmatrix} 0 \\ 0 \\ \sin\frac{\varphi}{2} \end{pmatrix}.$$

Therefore the QDFs $\boldsymbol{K}_{0,0}^{(\alpha_j=1/2)}$ are:

$$\boldsymbol{K}_{0,0}^{(\alpha_j)} = B_j \rho^{-1/2} \boldsymbol{\psi}_{0,j,0}, \qquad j = 1,2,3. \tag{C.3}$$

Taking

$$\boldsymbol{u} = A_{0_1}\rho^0\boldsymbol{\phi}_{0,0_1,0} + A_{0_2}\rho^0\boldsymbol{\phi}_{0,0_2,0} + A_{0_3}\rho^0\boldsymbol{\phi}_{0,0_3,0} \tag{C.4}$$

Substituting (C.4) and (C.3) in $Q_{\rho_0}\left[\boldsymbol{u}, \boldsymbol{K}_{0,0}^{(\alpha_{1,2,3}=1/2)}\right]$ with $B_1 = B_2 = -\frac{3(\lambda+\mu)}{64\pi^2 R\mu(\lambda+2\mu)}$ and $B_3 = \frac{1}{2\pi^2 R\mu}$ one obtains

$$Q_{\rho_0}\left[\boldsymbol{u}, \boldsymbol{K}_{0,0}^{(\alpha_1=1/2)}\right] = -A_{0_1}\frac{(9\lambda+2\mu)}{42\pi^2\mu}\frac{\sqrt{\rho}}{R} = \mathcal{O}\left(\frac{\sqrt{\rho}}{R}\right)$$

$$Q_{\rho_0}\left[\boldsymbol{u}, \boldsymbol{K}_{0,0}^{(\alpha_2=1/2)}\right] = -A_{0_2}\frac{5\lambda-2\mu}{14\pi^2\mu}\frac{\sqrt{\rho}}{R} = \mathcal{O}\left(\frac{\sqrt{\rho}}{R}\right)$$

$$Q_{\rho_0}\left[\boldsymbol{u}, \boldsymbol{K}_{0,0}^{(\alpha_3=1/2)}\right] = 0$$

Appendix D. The values of the extracted a_{j_q} for the inclined penny-shaped crack in a cube

Table D.13: The extracted coefficients of K_I, K_{II}, K_{III} by $Q_{\rho_0=0.1}[\boldsymbol{u}, \boldsymbol{K}_{0,0}^{(1/2)}]$

	$const$	$\cos\theta$	$\sin\theta$	$\cos 2\theta$	$\sin 2\theta$	$\cos 3\theta$	$\sin 3\theta$	$\cos 4\theta$	$\sin 4\theta$
K_I	4.2663E-01	-2.3802E-01	8.8985E-02	-3.8707E-02	2.8649E-02	6.2349E-03	5.7747E-03	9.2071E-04	2.9970E-03
K_{II}	-2.7674E-01	3.7675E-01	-6.5232E-02	-2.0040E-02	1.0162E-02	6.7109E-04	-5.8252E-03	-2.0649E-04	-1.0945E-03
K_{III}	-4.1192E-02	1.1710E-01	-2.0549E-01	3.2200E-02	3.2410E-02	-4.0250E-03	-1.6510E-03	-9.6340E-04	2.1308E-04

Table D.14: The extracted coefficients of K_I, K_{II}, K_{III} by $Q_{\rho_0=0.1}[\boldsymbol{u}, \boldsymbol{K}_{1,1}^{(1/2)}]$

	$const$	$\cos\theta$	$\sin\theta$	$\cos 2\theta$	$\sin 2\theta$	$\cos 3\theta$	$\sin 3\theta$	$\cos 4\theta$	$\sin 4\theta$
K_I	4.2737E-01	-1.1500E-01	8.1358E-02	-1.7252E-02	1.1115E-02	5.0005E-03	4.5736E-03	1.1285E-03	4.1211E-03
K_{II}	5.7558E-03	3.6916E-01	7.5537E-03	-2.0185E-02	1.0635E-02	3.2045E-04	-5.1922E-03	-1.4654E-04	-7.1171E-04
K_{III}	-4.0593E-02	2.0074E-02	-2.5049E-01	1.3255E-02	2.0369E-02	-5.1733E-03	-7.8239E-04	-8.7454E-04	1.9579E-04

Table D.15: The extracted coefficients of K_I, K_{II}, K_{III} by $Q_{\rho_0=0.1}[\boldsymbol{u}, \boldsymbol{K}_{2,2}^{(1/2)}]$

	$const$	$\cos\theta$	$\sin\theta$	$\cos 2\theta$	$\sin 2\theta$	$\cos 3\theta$	$\sin 3\theta$	$\cos 4\theta$	$\sin 4\theta$
K_I	4.3633E-01	-2.5474E-02	7.8526E-02	-1.0070E-02	3.7861E-03	4.5394E-03	4.0790E-03	1.1749E-03	4.3054E-03
K_{II}	-5.3593E-02	3.5138E-01	9.8270E-03	-2.3582E-02	1.6069E-02	7.4543E-04	-5.0210E-03	-1.6173E-04	-8.8043E-04
K_{III}	-3.9880E-02	1.9934E-02	-2.3347E-01	1.8186E-02	2.1701E-02	-3.2168E-03	-1.3137E-03	-7.9688E-04	1.0223E-04

Table D.16: The extracted coefficients of K_I, K_{II}, K_{III} by $Q_{\rho_0=0.1}[\boldsymbol{u}, \boldsymbol{K}_{3,3}^{(1/2)}]$

	$const$	$\cos\theta$	$\sin\theta$	$\cos 2\theta$	$\sin 2\theta$	$\cos 3\theta$	$\sin 3\theta$	$\cos 4\theta$	$\sin 4\theta$
K_I	4.3358E-01	-4.9469E-02	7.8258E-02	-3.8914E-03	-2.1030E-03	8.7098E-04	3.5500E-04	5.6592E-04	1.2567E-03
K_{II}	-2.5526E-02	3.4930E-01	1.8877E-02	-2.3950E-02	1.6576E-02	7.0836E-04	-4.9799E-03	-1.5220E-04	-8.1467E-04
K_{III}	-3.9792E-02	1.1110E-02	-2.3896E-01	1.1571E-02	1.7480E-02	-3.8102E-03	-6.7686E-04	-6.4577E-04	9.1637E-05

References

[1] A.A. Bakr. *The boundary integral equation method in axisymmetric sress analysis problems*. Springer, 1985.

[2] J.P. Benthem and W.T. Koiter. *Asymptotic Approximations to Crack Problems in Mechanics of Fracture (Edited by G.C. Sih)*. Noordhoff, Leyden, 1973.

[3] S.Y. Chen and T.N. Farris. Boundary elements crack closure calculation of axisymmetric stress intensity factors. *Computers & Structures*, 54:491–497, 1994.

[4] M. Costabel, M. Dauge, and Z. Yosibash. A quasidual function method for extracting edge stress intensity functions. *SIAM Jour. Math. Anal.*, 35(5):1177–1202, 2004.

[5] M. Dauge. *Elliptic boundary value problems in corner domains - smoothness and asymptotics of solutions*. Lecture notes in Mathematics 1341, Springer-Verlag, Heidelberg, 1988.

[6] L.A. De Lacerda and L.C. Wrobel. Dual boundary element method for axisymmetric crack analysis. *Int. Jour. Fracture*, 113:267–284, 2002.

[7] I. Demir, J.P. Hirth, and H.M. Zbib. The extended stress field around a cylindrical crack using the theory of dislocation pile-ups. *Int. Jour. Engrg. Sci.*, 30:829–845, 1992.

[8] R.J. Hartranft and G.C. Sih. The use of eigenfunction expansions in the general solution of three-dimensional crack problems. *Jour. Math. Mech.*, 19(2):123–138, 1967.

[9] T.K. Hellen. *Finite element energy methods in fracture mechanics*. PhD thesis, University of London, London, England, 1976.

[10] An-Yu Kuo. On the use of a path-independent line integral for axisymmetric cracks with nonaxisymmetric loading. *Trans. ASME, Jour. Appl. Mech.*, 54:833–837, 1987.

[11] J.B. Leblond and O. Torlai. The stress-field near the front of an arbitrarily shaped crack in a 3-dimensional elastic body. *Jour. of Elasticity*, 29(2):97–131, 1992.

[12] A.Y.T. Leung and R.K.L. Su. Eigenfunction expansion for penny-shaped and circumferential cracks. *Int. Jour. Fracture*, 89:205–222, 1998.

[13] J.J. Oglesby and O. Lomacky. An evaluation of finite element methods for the computation of elastic stress intensity factors. *Jour. Engineering for Indusry*, 95:177–185, 1973.

[14] N. Omer and Z. Yosibash. On the path independency of the point-wise J-integral in three-dimensions. *Int. Jour. Fracture*, 136:1 – 36, 2005.

[15] N. Omer, Z. Yosibash, M. Costabel, and M. Dauge. Edge flux intensity functions in polyhedral domains and their extraction by a quasidual function method. *Int. Jour. Fracture*, 129:97–130, 2004.

[16] S. Shannon and Z. Yosibash. Primal and shadow functions, dual and dual-shadow functions for a penny-shaped crack, cylindrical crack and external circular crack with Neumann boundary conditions. www.bgu.ac.il/˜zohary/PrimalShadows2013.pdf, 2013.

[17] S. Shannon, Z. Yosibash, M. Dauge, and M. Costabel. Extracting generalized edge flux intensity functions with the quasidual function method along circular 3-D edges. *Int. Jour. Fracture*, 181:25–50, 2013.

[18] I. N. Sneddon. The distribution of stress in the neighbourhood of a crack in an elastic solid. *Proc. Royal Soc. London. Series A. Math. Physical Sci.*, 187:229–260, 1946.

[19] T. von Petersdorff and E. P. Stephan. Decompositions in edge and corner singularities for the solution of the Dirichlet problem of the Laplacian in a polyhedron. *Math. Nachr.*, 149:71–103, 1990.

[20] M. L. Williams. Stress singularities resulting from various boundary conditions in angular corners of plates in extension. *Trans. ASME, Jour. Appl. Mech.*, 19:526–528, 1952.

[21] Z. Yosibash, N. Omer, M. Costabel, and M. Dauge. Edge stress intensity functions in polyhedral domains and their extraction by a quasidual function method. *Int. Jour. Fracture*, 136:37 – 73, 2005.

[22] Z. Yosibash, S. Shannon, M. Dauge, and M. Costabel. Circular edge singularities for the Laplace equation and the elasticity system in 3-D domains. *Int. Jour. Fracture*, 168:31–52, 2011.

[23] Z. Yosibash and B. A. Szabó. The solution of axisymmetric problems near singular points and computation of stress intensity factors. *Finite Elements in Analysis and Design*, 19:115–129, 1995.